A computational study of the influence of evaporation and molecular transport on temporally-evolving droplet-laden plane jets

Luis Antonio Carbajal Carrasco, Zakaria Bouali, Arnaud Mura

A computational study of the influence of evaporation and molecular transport on temporally-evolving droplet-laden plane jets

Luis Antonio Carbajal Carrasco, Zakaria Bouali, Arnaud Mura*

Institut Pprime, UPR3346 CNRS - ENSMA and University of Poitiers, France

Abstract

Numerical simulations of temporally-evolving droplet-laden plane jets are performed in conditions relevant to rocket main engines fed with liquid oxygen (LOx) and gaseous methane (CH_4). The computations are performed using a direct numerical simulation (DNS) solver with the liquid phase represented within the discrete particle simulation (DPS) framework. Considering the multiplicity of the physical phenomena that are involved in such conditions – e.g., atomization, dispersion, evaporation – a progressive and phenomenological methodology is retained to proceed with a complexity-increasing set of computations. Thus, the development of a purely gaseous jet is first studied with the corresponding set of data providing a reference or baseline condition. Then, other conditions are considered to analyze the influence of (i) liquid droplet evaporation and (ii) molecular mixing processes as described by two distinct multicomponent transport models. The analysis of the obtained results shows that both evaporation and molecular transport representation play a crucial role in the plane jet development and may drastically alter its characteristics before ignition and subsequent combustion stabilization may take place. Finally, the obtained results also unambiguously put into evidence the influence of the Lewis number onto the vaporization rate.

Keywords: plane jet, two-phase flow, dispersed phase, vaporization rate, molecular transport, Lewis number effect, direct numerical simulations

*Corresponding author, arnaud.mura@ensma.fr, tel: +33 5 49 49 81 80

1. General introduction

Since the early works of Townsend (1956), Bradbury (1965) or Bradbury and Riley (1967), the structure of unbounded turbulent plane wakes and jets has received considerable attention. Especially, experiments conducted on such turbulent free shear flows have confirmed the relevance of some self-similar features that characterize their spatial development. The corresponding flowfields have been also widely studied through computational studies. Thus, early computations of such turbulent plane jets were conducted in two dimensions, see for instance Comte et al. (1986), with special attention paid to vortex pairing and dynamics. More recently, the increase of computer performance has made possible performing three-dimensional numerical simulations of such plane jets until they reach their fully-developed turbulent state. With a few exceptions, e.g., Stanley et al. (2002), the corresponding numerical simulations were performed within the temporal framework and it must be emphasized that self-similarity does also apply to such temporally-evolving plane jets (Sadeghi et al., 2018).

In the present study, we analyze temporally-evolving turbulent plane jets but with one of the two streams seeded with liquid droplets. In this respect, it is noteworthy that the possible influence of a dispersed phase on free shear flow development has been previously studied by Dai et al. (2019a,b) who considered the case of compressible mixing layers seeded with solid particles. In contrast to these previous studies, some attention is presently paid to the influence of vaporization-induced mass transfer. Two different molecular mixing models are also used to analyze the possible effects of departures from the unity-Lewis assumption, an approximation that remains widely used in the modelling of turbulent reactive two-phase flows.

The manuscript is organized as follows: section 2 presents the retained geometry, flow conditions, computational methodology – with further details about the mathematical model provided in an appendix – and resulting set of numerical databases. Section 3 is focused on the description of the reference (i.e., baseline) gaseous case whereas the influence of the dispersed phase is studied in section 4. Finally, the manuscript is ended by a short section 5 where the possible effects of the molecular transport model are discussed before some conclusions are drawn and some perspectives are gathered in the last concluding section.

2. Problem description

2.1. Computational model

The new set of databases generated within the framework of the present study is constructed using the DNS-DPS solver `Asphodele`. This solver, the main features of which have been already presented else-

where (Reveillon et al., 2011), is based on a dilatable low-Mach number framework (Majda and Sethian, 1985). Within this framework, the pressure p is decomposed into two distinct contributions: the thermodynamic pressure p_0 and the dynamic pressure p_1. Indeed, as long as the flow velocity u remains sufficiently small with respect to the speed of sound c, in such a manner that the Mach number $\mathrm{M} = u/c$ remains smaller than 0.3, the pressure can be expanded as $p(\mathbf{x}, t) = p_0(t) + \gamma \mathrm{M}^2 p_1(\mathbf{x}, t) + O(\mathrm{M}^4)$, where γ denotes the heat capacity ratio, and $\gamma \mathrm{M}^2$ is a small parameter (significantly smaller than unity). The first contribution p_0, which is relevant to the equation of state (EoS), is spatially uniform whereas the second contribution p_1, which appears in the RHS of the momentum equation, may display spatial variations.

The resulting low-Mach number form of the Navier-Stokes equations is presented in Appendix A. Spatial derivatives are evaluated on regular meshes by making use of high-order precision finite difference schemes while time integration is carried out with a minimal storage third-order explicit Runge–Kutta scheme. The low-Mach number solver `Asphodele` is based on a quite standard projection algorithm with the density variation appearing through its first-order temporal derivative in the RHS of the Poisson's equation and this derivative being evaluated using a strategy similar to the one introduced by Cook and Riley (1996). The resolution of the Poisson's equation makes use of the `HYPRE` library (Falgout and Yang, 2002). The dispersed liquid phase, which is described from a Lagrangian point of view, is solved within the particle-source in cell (PSI-cell) framework (Crowe et al., 1977). The interested reader may found futher details in Appendix A and in the previous work of Zhao et al. (2020).

2.2. Computational setup and associated velocity field

The computational geometry is inspired by the one previously considered by Abdelsamie and Thevenin (2017). A rectangular computational domain is considered. Periodic boundary conditions are prescribed along all directions. The streamwise, vertical, and spanwise directions are hereafter denoted by x_1, x_2, and x_3, respectively. The initial velocities (i.e., at $t = 0$) of the central jet and coflowing stream are referred to as U_1 and U_2, respectively, where $\mathrm{U}_2 < \mathrm{U}_1$. Thus, the initial value of the convective velocity is $\mathrm{U}_c \equiv u_c(t = 0) = (\mathrm{U}_1 + \mathrm{U}_2)/2$ and the one of the velocity difference between the central jet and coflowing stream is $\Delta\mathrm{U} \equiv \Delta u(t = 0) = \mathrm{U}_1 - \mathrm{U}_2$. At this level, it is worth emphasizing that, in the present work, upper case letters refer to initial values, whereas lower case letters denote instantaneous values. The initial jet thickness H is defined as twice the characteristic half-width of the initial streamwise velocity profile $\mathrm{H} \equiv 2\,\delta^0_{0.5} = 0.715$ mm. Finally, droplets are randomly scattered within the central part of the jet. The initial velocity of each droplet matches the surrounding flow velocity, i.e., at $t = 0$, no slip velocity is considered

between the droplets and the gas carrier phase. A simplified representation of the retained computational setup is depicted in Fig. 1.

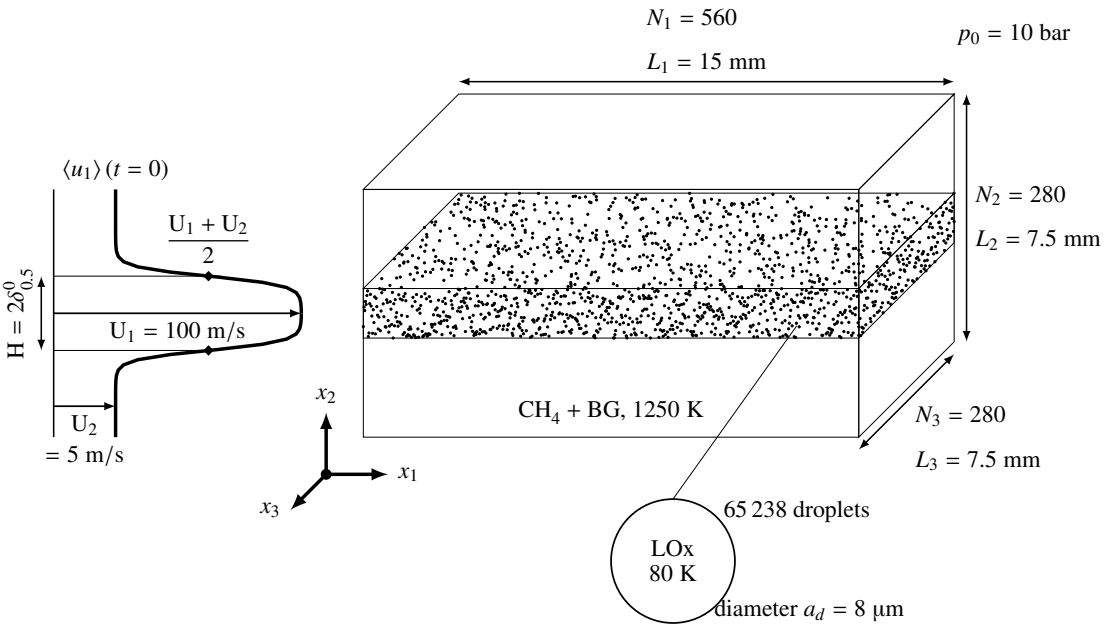

Figure 1: Sketch of the computational setup. The acronym BG refers to burned gases issued from the combustion of a stoichiometric mixture of methane in pure oxygen.

The characterization of the developing plane jet makes use of the convective velocity

$$u_c(t) = \frac{1}{2}\left(\max_{x_2}\left(\langle u_1 \rangle (x_2, t)\right) + \min_{x_2}\left(\langle u_1 \rangle (x_2, t)\right)\right) \tag{1}$$

together with the velocity difference between the central jet and coflowing stream

$$\Delta u(t) = \max_{x_2}\left(\langle u_1 \rangle (x_2, t)\right) - \min_{x_2}\left(\langle u_1 \rangle (x_2, t)\right) \ . \tag{2}$$

where $\langle \varphi \rangle$ denotes the Reynolds-averaged value of any quantity φ.

Averaging is performed along the streamwise and spanwise directions (Taguelmimt et al., 2016; VanDine et al., 2020), i.e., in horizontal planes. Thus, the average of any quantity φ is evaluated from:

$$\langle \varphi \rangle (x_2, t) = \int_0^{L_1} \int_{-L_3/2}^{L_3/2} \varphi(x_1, x_2, x_3, t) dx_3 dx_1 \Big/ (L_1 L_3) \ , \tag{3}$$

and the corresponding fluctuation is $\varphi' = \varphi - \langle \varphi \rangle$.

The vertical and spanwise velocity component (u_2 and u_3) are initially set to zero, whereas the value of the longitudinal component is initialized using a hyperbolic function:

$$u_1(x_1, x_2, x_3, t = 0) = (\mathrm{U}_1 + \mathrm{U}_2)/2 + (\mathrm{U}_1 - \mathrm{U}_2)/2 \cdot \tanh\left(2\left(\delta^0_{0.5} - |x_2|\right)/\delta^0_\omega\right) \quad (4)$$

$$= \mathrm{U}_c + \Delta\mathrm{U}/2 \cdot \tanh\left(2\left(\delta^0_{0.5} - |x_2|\right)/\delta^0_\omega\right) \ . \quad (5)$$

The quantities $\delta^0_{0.5} \equiv \delta_{0.5}(t = 0)$ and $\delta^0_\omega \equiv \delta_\omega(t = 0)$ refer to the initial values of the jet half-width $\delta_{0.5}$ and vorticity thickness $\delta_\omega = \Delta\mathrm{U}/|\partial \langle u_1 \rangle_f / \partial x_2|_{\max}$, respectively. The jet half-width $\delta_{0.5}(t)$ is defined by $\langle u_1 \rangle (\delta_{0.5}, t) = \langle u_1 \rangle (-\delta_{0.5}, t) = u_c(t)$. At this level, it is worth noting that, even if the retained configuration features a symmetry plane at $x_2 = 0$, the above definitions may lead to different values of the half-width and vorticity thickness depending on whether the formulas are applied to the upper or lower parts of the plane jet. Therefore, unless otherwise stated, for each these characteristic length scales, the arithmetic mean of the upper and lower values is considered. The transition of the plane jet is obtained using a low-amplitude perturbation (white noise) that is superimposed on the transverse and spanwise velocity components (Carbajal Carrasco, 2021). Such perturbations are indeed prone to trigger the development of the plane jet natural instability modes. Their amplitude was presently set to 0.2 percent of the convective velocity.

As mentioned above, the computational conditions have been chosen to be representative of the ignition phase of rocket main engines. This ignition phase takes place at moderate pressure, i.e., below the nominal value of the combustion chamber operating pressure, and thus it does not require the consideration of some high pressure (supercritical) effects that have been discussed elsewhere (Candel et al., 1998; Yang, 2000; Oefelein, 2005; Demoulin et al., 2009). Thus, the value of p_0 has been set to 10 bars, a value that is typical of rocket engine ignition computation (Gomet et al., 2014). The fuel (i.e., methane) is at its gaseous state whereas the oxidizer (pure oxygen) is at its liquid state. Primary and secondary atomization of the liquid oxygen jet is not considered and a monodisperse spray of liquid oxygen (LOx) droplets is considered. The gas is a mixture of methane and residual burned gases (BG) issued from the combustion of a stoichiometric CH_4/O_2 mixture. The total mass of burnt gases corresponds to thirty percent of the total mass of fresh reactants (methane plus liquid oxygen). It should also be pointed out that the spatial discretization is uniform along the three directions $\Delta x = \Delta x_1 = \Delta x_2 = \Delta x_3$ with Δx approximately equal to 27 μm. In this respect, the liquid droplet diameter a_d satisfies the condition $a_d/\Delta x < 0.3$. Thus, its values fulfills the criterion $a_d/\Delta x < 0.6$, which is commonly retained to proceed with DNS-DPS simulations in the literature (Wang and Rutland, 2007; Neophytou et al., 2011; Wang et al., 2014). It is also noteworthy that the global value

of the liquid volume fraction and liquid mass fraction are significantly smaller than unity. Especially, the global value of the liquid volume fraction is $\Phi_v = 2.07 \cdot 10^{-5}$, which is relevant to the dilute regime and fully consistent with the number of liquid droplets per computational cell that ranges between zero and two. The ratio of the liquid and gas density is 993.90. Finally, according to Balachandar and Eaton (2010), it must also be emphasized that, since the ratio of the particle diameter to Kolmogorov scale[1] is of the order of one tenth and the liquid volume fraction quite small, the carrier-phase turbulence is expected to be nearly the same as the equivalent single-phase flow.

At this level, it must be emphasized that simulations of turbulent two-phase flows with evaporation, such as those performed for the purpose of the present study, are subject to several constraints that are difficult to accommodate and the possible influence of grid refinement remains a source of questioning. From a more general point of view, two-phase flow DNS would formally require full grid resolution both in and around each liquid droplets. For instance, such DNS computations have been recently performed (i) to study how a reduced set of possibly vaporizing liquid droplets (or blobs) modifies the turbulent flow field topology (Onofre Ramos et al., 2022a) or (ii) to analyse the influence of evaporation on scalar mixing in the gas phase (Onofre Ramos et al., 2022b; Germes Martinez et al., 2023). The associated changes result from interactions between the two phases (liquid and gas) at scales that are smaller than the droplet size. The corresponding processes are not resolved through discrete particle simulations (DPS) conducted within a Lagrangian framework such as those considered herein. However, when the computational study is concerned with the evaporation of spray jets – possibly followed by chemical reactions – featuring an important number of droplets and with a focus placed on larger scale features of spray-gas interaction and dispersion, performing DNS computations such as those mentioned above (Onofre Ramos et al., 2022a; Germes Martinez et al., 2023) still remains rather impractical. In such cases, another approach consists in simulating the gas-phase carrier fluid with a high-resolution Eulerian method, while the liquid droplets are simulated within a Lagrangian particle framework. This is the approach that has been retained for the purpose of the present study and it is herein referred to as DNS-DPS where DPS stands for discrete particle simulation. The DNS terminology is used because, despite flows inside the droplets or their immediate wake regions not being resolved, the gas-phase flow is highly resolved without any resort to a turbulence model. This approach allows studies of sprays featuring a large number of droplets with a focus placed on larger scale features of spray–gas interaction and mixing.

[1]This value will be evaluated in the next section.

Thus, in spray combustion computational solvers – such as the one retained for the purpose of the present study – the Euler-Lagrange (EL) approach remains a common strategy for simulating the reactive two-phase flow. The coupling between the continuous (gas) and dispersed (liquid) phases is achieved through the introduction of source terms[2] in the Eulerian transport equations that are solved for the gas phase, while the effect of the gas phase is considered through the specification of boundary conditions relevant to the gas film around droplets (or groups of droplets). At this level, it must be emphasized that, with few exceptions (e.g., Akiki et al. (2017)), the later mostly relies on the picture of a single (isolated) droplet in an homogeneous gaseous media, with the corresponding models incorporating some possible corrections. "Ambient-gas" conditions are thus required to determine the droplet vaporization rate, heating rate, and drag. The corresponding theoretical models do involve conditions at the edge of the gas film. However, the neighboring computational points may lie inside the gas film. Especially, in the case of DNS-DPS computations – such as those conducted for the purpose of the present study – grid points lie in the direct vicinity of droplets. Such limitations have been early emphasized by Rangel and Sirignano (1989) for the evaluation of the vaporization rate. This raises the issue of coupling terms convergence under mesh refinement (Gualtieri et al., 2013; Capecelatro and Desjardins, 2013). Indeed, in regard to the drag force, as deduced from a Stokes law that considers single spherical particles, its determination does involve the gas velocity conditions "at infinity", i.e., sufficiently far from the region perturbed by the particle motion. In this respect, it must be emphasized that the present set of computations has been conducted considering the two-way couplings between the gas and liquid droplets but within a standard particle in cell (PIC) framework. However, it should indeed be acknowledged that, within such a framework, the back-reaction of the particle on the fluid has been shown to be grid-dependent. Thus, one possible direction for future developments of our computational model would consist in improving the accuracy of the Stokes drag determination (Horwitz and Mani, 2016; Ireland and Desjardins, 2017; Esmaily and Horwitz, 2018) and possible influence of neighboring droplets (Akiki et al., 2017).

Finally, the value of the Stokes number St, presently defined as $\mathrm{St} = \tau_{V_d} \Delta u / \delta_{0.5}$ with τ_{V_d} the droplet relaxation time (Hu et al., 2002), is $\mathrm{St} = 25$. At this level, it is noteworthy that other definitions of St are available in the literature but the one provided above seems to be the best suited for the purpose of the present study devoted to plane jets.

[2]The detailed expressions of these source terms are provided in Appendix A.

2.3. Characterization of the multicomponent mixture composition

The composition of reactive multicomponent mixtures is standardly characterized through the use of the mixture fraction variable (Bilger, 1976; Peters, 1984). Indeed, provided that the differences in the molecular diffusion coefficient remain negligible from one chemical species to another – i.e., unity Lewis number approximation – the mixture composition is unambiguously characterized through the single knowledge of the mixture fraction value.

From a general point of view, the mixture fraction is a conserved scalar that is bounded between zero (in the oxidizer) and unity (in the fuel). It can be thought as a fuel inlet tracer (Gomet et al., 2015) that provides, at any time and location, the proportion of mass that is issued from the fuel inlet stream. It can be defined on the basis of the number of retained chemical species (or molecules) N_s and number of corresponding atoms N_a. In addition to this, introducing the quantity Γ as a subset of N_a containing only n_a atomic species, the mixture fraction associated to the subset Γ is defined as

$$\xi_\Gamma = \sum_{\beta=1}^{n_a} b_{\Gamma,\beta} \cdot (Z_\beta - Z_{\beta,ox}) \Big/ \sum_{\beta=1}^{n_a} b_{\Gamma,\beta} \cdot (Z_{\beta,fuel} - Z_{\beta,ox}) \,, \tag{6}$$

where Z_β is the mass fraction of the atomic species β. The indexes $fuel$ and ox refer to the values taken in the fuel and oxidizer streams, respectively. For each subset Γ, weighting coefficients $b_{\Gamma,\beta}$ are introduced. It is straightforward that, for any set of weights that satisfies the condition $\sum_{\beta=1}^{n_a} b_{\Gamma,\beta}(Z_{\beta,fuel} - Z_{\beta,ox}) \neq 0$, the expression given by Eq. (6) ensures $\xi_{\Gamma,ox} = 0$ and $\xi_{\Gamma,fuel} = 1$.

For instance, a simple definition of the mixture fraction can be obtained by considering the subset $\mathrm{O} = \{\mathrm{O}\}$, which leads to:

$$\xi_\mathrm{O} = (Z_\mathrm{O} - Z_{\mathrm{O},ox})/(Z_{\mathrm{O},fuel} - Z_{\mathrm{O},ox}) \,. \tag{7}$$

This definitions corresponds to a mixture fraction definition based on the oxygen atom conservation.
For the subset $\mathrm{B} = \{\mathrm{C}, \mathrm{H}, \mathrm{O}\}$ and using values of $b_{\Gamma,\beta}$ such that $b_{\mathrm{B,C}} = 2(W_\mathrm{C})^{-1}$, $b_{\mathrm{B,H}} = (2W_\mathrm{H})^{-1}$, and $b_{\mathrm{B,O}} = -(W_\mathrm{O})^{-1}$, the following expression is obtained:

$$\xi_\mathrm{B} = \frac{2(Z_\mathrm{C} - Z_{\mathrm{C},ox})/W_\mathrm{C} + (Z_\mathrm{H} - Z_{\mathrm{H},ox})/(2W_\mathrm{H}) - (Z_\mathrm{O} - Z_{\mathrm{O},ox})/W_\mathrm{O}}{2(Z_{\mathrm{C},fuel} - Z_{\mathrm{C},ox})/W_\mathrm{C} + (Z_{\mathrm{H},fuel} - Z_{\mathrm{H},ox})/(2W_\mathrm{H}) - (Z_{\mathrm{O},fuel} - Z_{\mathrm{O},ox})/W_\mathrm{O}} \,, \tag{8}$$

which is nothing but Bilger's mixture fraction definition (Bilger et al., 1990).

By taking into account the specificity of the retained configuration, namely, a plane jet where the main stream is a mixture of fuel and burnt gases, whereas oxidizer is available in the form of a spray of LOx droplets, the choice of the mixture fraction definition is not trivial. Therefore, the relevance of the two

definitions provided above – i.e., Eqs.(7) and (8) – will be studied. In this respect, it should be pointed out that the range of variation of the oxygen mass fraction is constrained by the vaporization process in the sense that its theoretical maximum value corresponds to the saturation condition $Y^S_{O_2}$. Therefore, the oxidizer stream atomic mass fraction is set in such a manner that it satisfies the saturation condition

$$Z_{O,ox} = 2Y^S_{O_2}\frac{W_O}{W_{O_2}} + \sum_{\alpha\neq O_2} a_{O,\alpha}Y_{\alpha,ox}\frac{W_O}{W_\alpha} \tag{9}$$

	Nomenclature	Meaning
Molecular transport	`LeU`	Unity Lewis number
	`LeNU`	Non-unity Lewis number
Dispersed phase	`PEV`	Pre-vaporized
	`NEV`	Non-vaporizing
	`EV`	Vaporizing

Table 1: DNS database nomenclature.

2.4. Description of the DNS database

A nomenclature is introduced so as to discriminate each computational conditions, see Tab. 1. The classification is based on (i) the multicomponent molecular transport model and (ii) the dispersed phase representation with three possible cases: pre-vaporized, non-evaporating droplets, and finally evaporating droplets. It is noteworthy that "pre-vaporized" refers to a case with the droplet evaporation assumed to be infinitely fast: the corresponding cases (`LeU-PEV` and `LeNU-PEV`) are purely gaseous but feature a gas composition that accounts for the corresponding mass of oxygen. Thus, the resulting database includes six distinct cases, see Tab. 2.

`LeU`	`LeU-PEV`	`LeNU-PEV`
`LeU-NEV`	`LeU-EV`	`LeNU-EV`

Table 2: DNS database constitution.

Finally, it should also be pointed out that the configuration `LeU` does not take into account the dispersed phase: it corresponds to a purely gaseous condition featuring a homogeneous composition. This configuration is retained as a reference so as to evaluate the impact of the liquid phase on the multicomponent

flowfield. To summarize, three gaseous cases (LeU, LeU-PEV, and LeNU-PEV) are considered together with three two-phase flow cases (LeU-NEV, LeU-EV, and LeNU-EV).

3. Reference case

The present section is aimed at providing some information on the plane jet development in the reference (baseline) LeU case before embarking on possible effects induced by mass transfer (molecular diffusion representation and/or vaporization).

3.1. Mixing layer growth during the potential core phase

Figure 2 depicts the evolution of the vorticity thickness δ_ω as a function of the normalized time $\tau_\omega = t\Delta U/\delta_{\omega,0}$. As emphasized in the previous section, different values of the vorticity thickness may be obtained in the upper and lower parts of the plane jet. Provided that the mean velocity profile is symmetric, both values should be identical. The presence of slight disparities in the velocity profile may however induce some differences in the corresponding upper and lower evolutions. For the sake of consistency, only the time-steps relevant to the potential core phase, further detailed below, are considered.

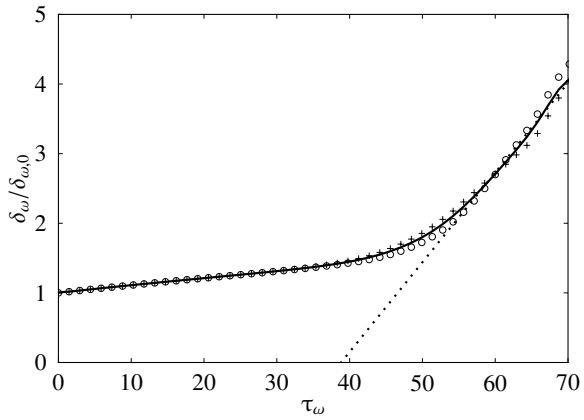

Figure 2: Temporal evolution of the normalized vorticity thickness. + upper part of the jet; ∘: lower part. Solid line: mean evolution. Dashed: linearized evolution.

Between $\tau_\omega = 0.0$ and $\tau_\omega = 70.0$, both estimates of the vorticity thickness follow a standard evolution, which is rather similar to the one observed in temporally-evolving mixing layers. It is noteworthy that the corresponding evolution is linear, which is relevant to self-similarity.

In the case of temporally-evolving mixing layers, this evolution is characterized on the basis of the normalized growth-rate $\dot{\delta}_\omega = (d\delta_\omega/dt)/\Delta U$. In the present case, it is $\dot{\delta}_\omega = 0.065$. In order to make easier the comparison of the present results with those previously obtained for spatially-evolving mixing layers, it is possible to approximate the growth-rate of an equivalent spatially-developing mixing layer $\delta'_{\omega,x}$ as follows

$$\delta'_{\omega,x} = \frac{1}{\eta}\frac{d\delta_\omega}{dx_1} = \frac{U_1 + U_2}{U_1 - U_2}\frac{d\delta_\omega}{dx_1} = \frac{1}{\eta}\frac{dt}{dx_1}\frac{d\delta_\omega}{dt} = \frac{2}{\Delta U}\frac{d\delta_\omega}{dt} = 2\dot{\delta}_\omega \ . \tag{10}$$

In the above expression, the parameter η is given by $(U_1 - U_2)/(U_1 + U_2) = \Delta U/(2U_c)$ and it has been assumed that the temporal window is moving at the convective velocity $U_c = (U_1 + U_2)/2$. With this definition, it is possible to compare the present results to those previously reported for incompressible mixing layers. The corresponding values are summarized in Tab. 3.

Reference	Type	$\delta'_{\omega,x}$
Spencer and Jones (1971)	Exp.	0.160
Wygnanski and Fiedler (1970)	Exp.	0.190
Stanley and Sarkar (1997)	DNS-2D	0.143
Martínez Ferrer et al. (2017)	DNS-2D	0.166
Bogey (2000)	DNS-2D	0.180
Rogers and Moser (1994)	DNS-3D	0.130
Bell and Mehta (1990)	DNS-3D	0.163
Present work: case `LeU`	DNS-3D	0.130

Table 3: Normalized growth-rate of different incompressible mixing layers.

Finally, it appears that, during the potential core phase, the growth-rate of the mixing layers relevant to the upper and lower parts of the plane jet is quite similar to the one documented for mixing layers. Then, both mixing layers begin to interact and this interaction marks the beginning of a new phase that will be referred to as the auto-similarity phase.

3.2. Flow development during the auto-similarity phase

The temporal evolution of the jet is now followed according to a normalized time $\tau_{0.5}$, which is defined on the basis of the jet half-width, i.e., $\tau_{0.5} = t\Delta U/\delta^0_{0.5}$. As emphasized above, sheared flows are known to display some auto-similar characteristics (Townsend, 1956). Especially, in plane jets, auto-similarity can be put into evidence by recasting the mean streamwise velocity component into the product of a characteristic

velocity u_s (Bradbury, 1965) – which is only time-dependent – and a function f that depends only on a normalized spatial coordinate x_2/l_s:

$$\langle u_1 \rangle (x_2, t) = u_s(t)\, f(x_2/l_s) \tag{11}$$

In general, the values of u_s and l_s are set to u_c and $\delta_{0.5}$, respectively. At this level, it is noteworthy that, in most of the studies, the retained characteristic velocity is the jet centerline velocity and not the convective velocity as defined by Eq. (1). However, it must be emphasized that, in the corresponding configurations, the jet exits into a quiescent medium and/or the computational domain is sufficiently large, in such a manner that the coflowing stream velocity U_2 remains constant. In such conditions, the jet centerline velocity may be readily expressed as a function of the convective velocity by using a Galilean transform. Finally, recent study by Sadeghi et al. (2018) established that the use of such auto-similarity laws, which may seem empirical at first sight, can be more formally justified.

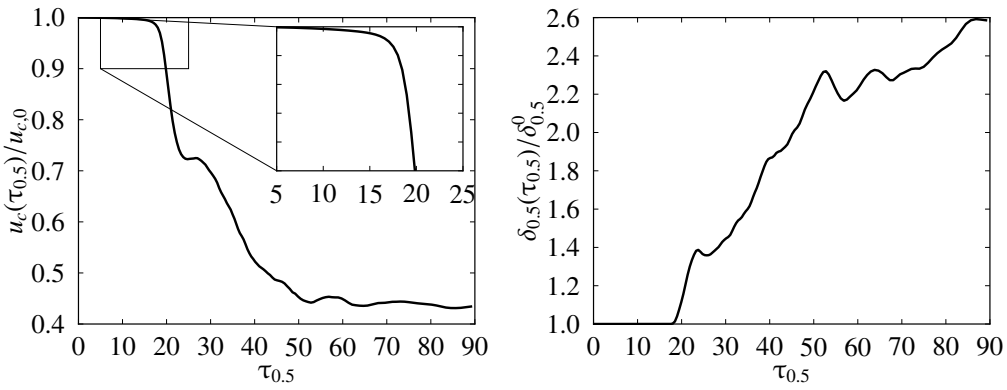

Figure 3: Temporal evolution of the normalized convective velocity u_c (left) and half-width $\delta_{0.5}$ (right).

The temporal evolution of the aforementioned functions is depicted in Fig. 3. The persistence of the potential core can be readily delineated at the early stages of the plane jet development. The normalized convective velocity and half-width indeed remain almost unchanged with respect to their initial values: the two shear layers that develop on the plane jet boundaries behave as independent mixing layers. In the present case, this behaviour is observed until $\tau_{0.5}$ is approximately equal to seventeen, a value quite similar to the value $\tau_{0.5} = 16.9$ previously documented by Bogey and Pineau (2018) in their study of a temporally-evolving low-Mach number round jet. The potential core phase is followed by a sharp decay of the velocity and the auto-similarity phase begins. The possible self-similarity of the flow development is

now evaluated on the cross-stream profiles of the mean longitudinal velocity component $\langle u_1 \rangle$, see Fig. 4. The corresponding data are collected after the jet potential core phase. On the left side of this figure, the values of the abscissa x_2 and mean velocity $\langle u_1 \rangle$ are simply normalized by the initial half-width and convective velocity, respectively, and the corresponding profiles obviously display a non-negligible scatter. This is in contrast with the results issued from a normalization that makes use of u_c and $\delta_{0.5}$ in Eq. 11. Indeed, once normalized, all profiles collapse onto a single bell-shaped function. Slight departures from self-similarity may however be observed at the bases of these normalized profiles. This may be explained by the presence of some perturbations in the vicinity of $\tau_{0.5} = 25.0$, see Fig. 3. Therefore, the values $\tau_{0.5} = 18.0$ and $\tau_{0.5} = 25.0$ are retained as relevant boundaries to perform auto-similarity analyses.

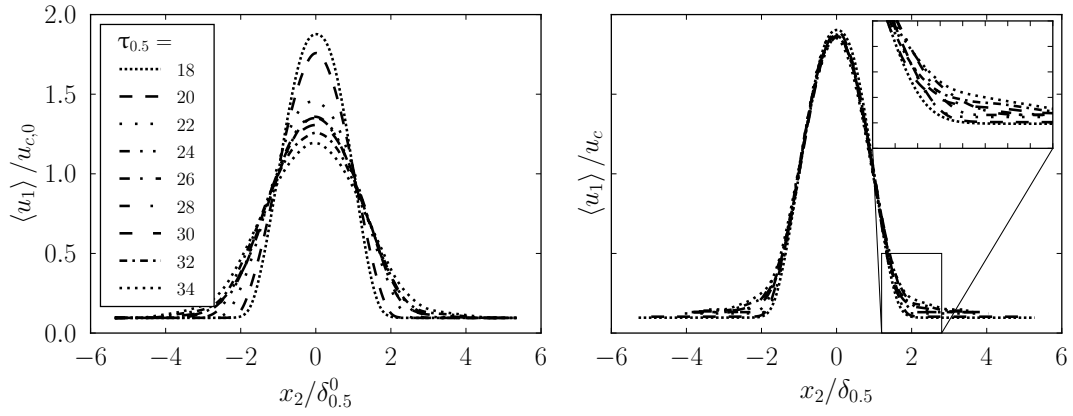

Figure 4: Left: profiles of the mean streamwise velocity component $\langle u_1 \rangle$ plotted versus x_2, values are normalized by the initial half-width and convective velocity. Right: profiles normalized using the auto-similarity functions. Nine profiles equi-distributed between $\tau_{0.5} = 18.0$ and 34.0.

Spatially-developing plane jets display a direct proportionality between their thickness and the inverse of their squared centerline velocity (Schlichting, 1968). A similar proportionality holds between their squared convective velocity u_c^2 and the inverse of their half-width $1/\delta_{0.5}$, see for instance Gordeyev and Thomas (2000) or Stanley et al. (2002). This is in contrast to their temporally-developing counterparts, which are characterized by a convective velocity that is inversely proportional to their half-width (Sadeghi et al., 2018). The evolution reported in Fig. 5 indeed confirms this tendency: the ratio $u_{c,0}/u_c$ is found to be approximately equal to $\delta_{0.5}/\delta^0_{0.5}$, provided that the latter remains smaller than 2.2. This limit in the domain of variation of $\delta_{0.5}/\delta^0_{0.5}$ is an outcome of the computational domain dimensions: the close proximity of the boundary conditions indeed induces some departures from linearity.

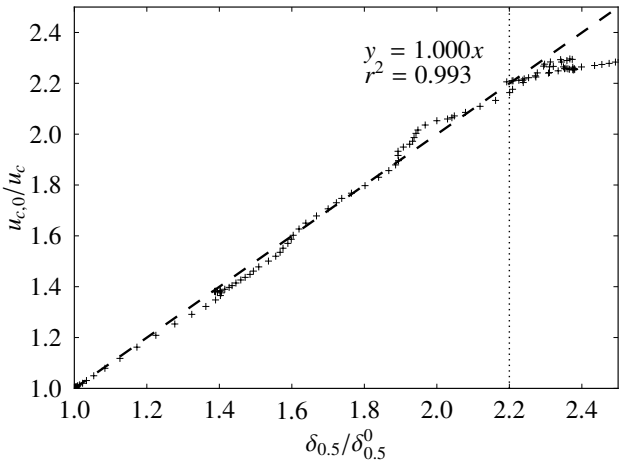

Figure 5: Inverse of the convective velocity u_c versus half-width $\delta_{0.5}$. Dashed line: linear evolution up to $\delta_{0.5}/\delta^0_{0.5} = 2.2$ ($\tau_{0.5} = 50$).

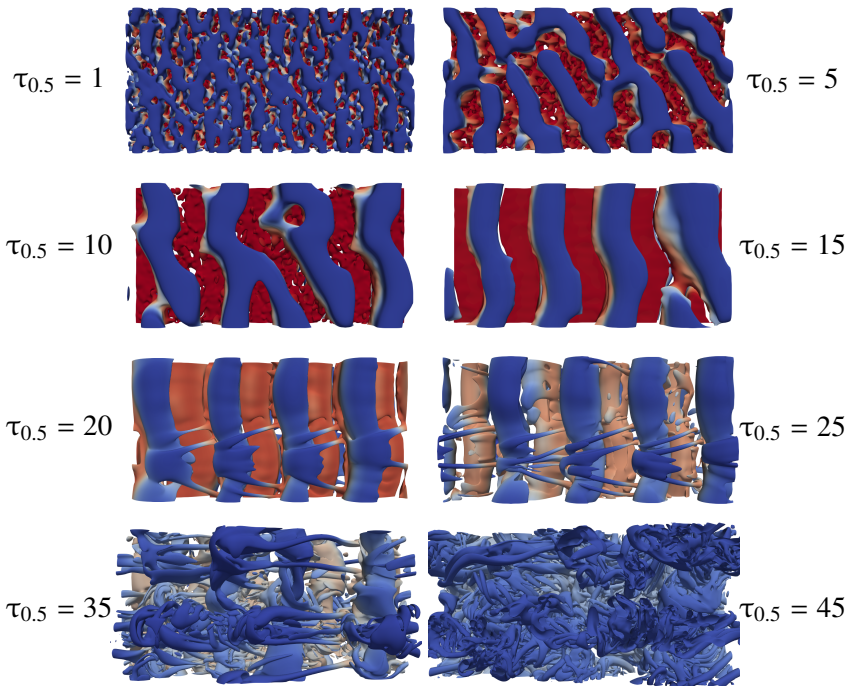

Figure 6: Top view – whole computational domain – of the iso-contour of the second invariant of the VGT $Q/Q_{\max} = 0.001$ (approximately $0.01 \times \Delta u/\delta_{0.5}$) colored with the value of the longitudinal velocity component u_1. Case `LeU`.

The plane jet development can be pictured on the basis of some criteria that are commonly used to identify flow structures (Lesieur et al., 2005), see Appendix B. For instance, an iso-contour of the second invariant Q of the velocity gradient tensor (VGT) is depicted in Fig. 6 for different time steps. In the early stages, it is rather difficult to delineate coherent structures and, in this regard, it seems worth reminding that a white noise was initially used to trigger the development of Kelvin-Helmholtz instability. Later on, and especially from $\tau_{0.5} = 15.0$, large coherent structures can be delineated.

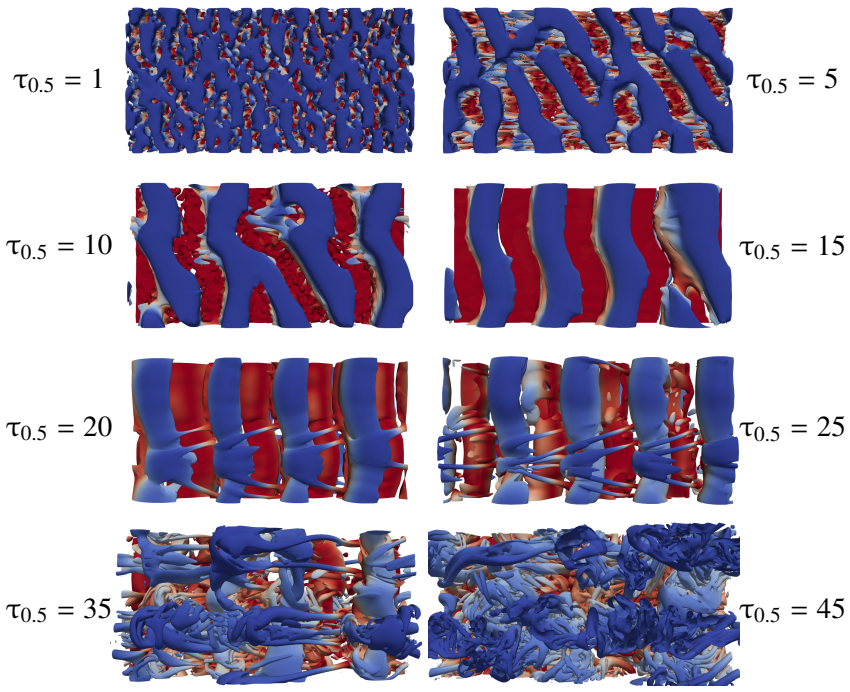

Figure 7: Top view – whole computational domain – of the iso-contour $\lambda_2/\lambda_{2,\max} = 0.001$ colored with the value of the longitudinal velocity component u_1. Case `LeU`.

Two sets of tube-shaped vortices do appear with one set located on the upper part of the jet and another located on its lower part. The two sets start developing independently from each other. Subsequently, between $\tau_{0.5} = 15.0$ and $\tau_{0.5} = 20.0$, the upper and lower sets start to interact, and this interaction marks the end of the potential core stage. Tri-dimensional effects become visible with the birth of hairpin-shaped vortices (Bernal and Roshko, 1986) and this may induce some dissymetries in the mean velocity profile. Finally, when the largest structures collapse ($\tau_{0.5} \geq 45.0$), the flow structure seems to be more "chaotic", which sign its transition to turbulence. A similar behavior is observed through the consideration of the λ-criterion instead of the Q-criterion, see Fig. 7. However, with this criterion, the footprint of the hairpin

vortices is visualized slightly early.

3.3. Towards developed turbulence?

The transitional flow is now inspected on the basis of its small-scale characteristics. Indeed, at latter stages of its development (i.e., $\tau_{0.5} > 120.0$), the flow topology features some characteristics that are closer to those of homogeneous turbulence. For instance, this is visible of the joint statistics of second and third invariants of the VGT that are reported in Fig. 8. The corresponding distribution indeed displays a tear-drop shape similar to the one early reported by Ooi et al. (1999) in the case of homogeneous isotropic turbulence (HIT). This feature is indeed typical of many types of turbulent flows including sheared turbulence (Tsinober, 2009). It is also relevant to turbulent two-phase flows provided that the VGT statistics are collected in the carrier phase (Onofre Ramos et al., 2022a).

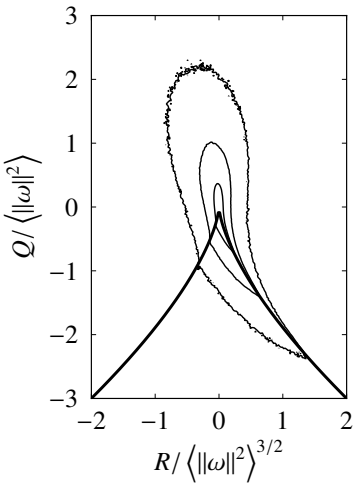

Figure 8: Iso-lines of the joint PDF of the second and third VGT invariants (Q and R) normalized by the vorticity norm. The spacing between consecutive iso-lines is one decade and decade exponents are, from outer to inner: -2, -1, and 0.

At this level, the size of the computational domain as well as the numerical resolution deserve to be analyzed in further details. To this purpose, the computational domain dimensions are compared to the turbulent scales in order to verify that: (i) the extents in the streamwise and spanwise directions are large enough to capture the largest length scales, and that (ii) the smallest scales, as given by the Kolmogorov scaling, are properly solved. Two different methods can be used in conjunction with scaling relationships in order to evaluate turbulent scales (Pope, 2000). In the first approach, integral length scales are deduced from the two-point correlation computations, whereas the second approach makes use of the computed turbulent

kinetic energy $\langle k \rangle$ and dissipation rate $\langle \varepsilon \rangle$:

$$\ell_t = \langle k \rangle^{3/2} \langle \varepsilon \rangle^{-1} \quad \text{and} \quad \eta_K = \langle \nu \rangle^{3/4} \langle \varepsilon \rangle^{-1/4} \ . \tag{12}$$

where ℓ_t and η_K denote the integral and Komogorov length scales, respectively. The averaging is performed for values of the normalized times $\tau_{0.5}$ that are larger than 120.

For any quantity φ, the two-point correlation along the direction x_i can be expressed as follows:

$$R_{i,\varphi}(\Delta x_i, x_2, t) = \left\langle \varphi'(x_1, x_2, x_3, t) \varphi'(x_1 + \delta_{1i}\, \Delta x_i, x_2, x_3 + \delta_{3i}\, \Delta x_i, t) \right\rangle / \left\langle \varphi'^2 \right\rangle \ , \tag{13}$$

where δ_{1i} denotes the Kronecker delta operator.

Figure 9 reports two-point correlations of the velocity field components along the longitudinal and spanwise directions. Five locations are considered along the x_2 direction: the jet center-line, the two shearing interfaces, and locations close to the boundary condition, with one point on each side (upper and lower parts) of the plane jet. As expected, the correlation decreases as the distance Δx_i between the two points is increased and the small values obtained at large abscissa (i.e., in the middle of the domain) confirms that there is no remarkable contamination of the results by finite domain size effects.

Turbulence integral length scales along the spanwise and streamwise directions can be deduced from these correlations (Pope, 2000):

$$\ell_{t,i} = \int_0^{L_i/2} R_{i,u_i} d(\Delta x_i) \ . \tag{14}$$

The values of the integral length scales, as evaluated from Eq. (12) and Eq. (14), are reported in Tab. 4. The obtained results show that the integral length scales remain of the order of one tenth of the extent of the computational domain, which is fully consistent with values previously documented in other references (Pantano and Sarkar, 2002; Pantano et al., 2003; Mahle, 2007). Moreover, the ratio between the streamwise and spanwise integral length scale is close to two, a rather standard value for this kind of flow configuration (Pope, 2000). Finally, it is noteworthy that the estimates deduced from Kolmogorov scalings, as given by Eq. (12) , are slightly smaller than those deduced from the correlation function.

	$\ell_{t,1}/\ell_{t,3}$	$\ell_{t,1}/L_1$	$\ell_{t,3}/L_3$
Eq. (12)	1.70	0.078	0.092
Eq. (14)	1.76	0.132	0.149

Table 4: Integral length scales versus domain dimensions.

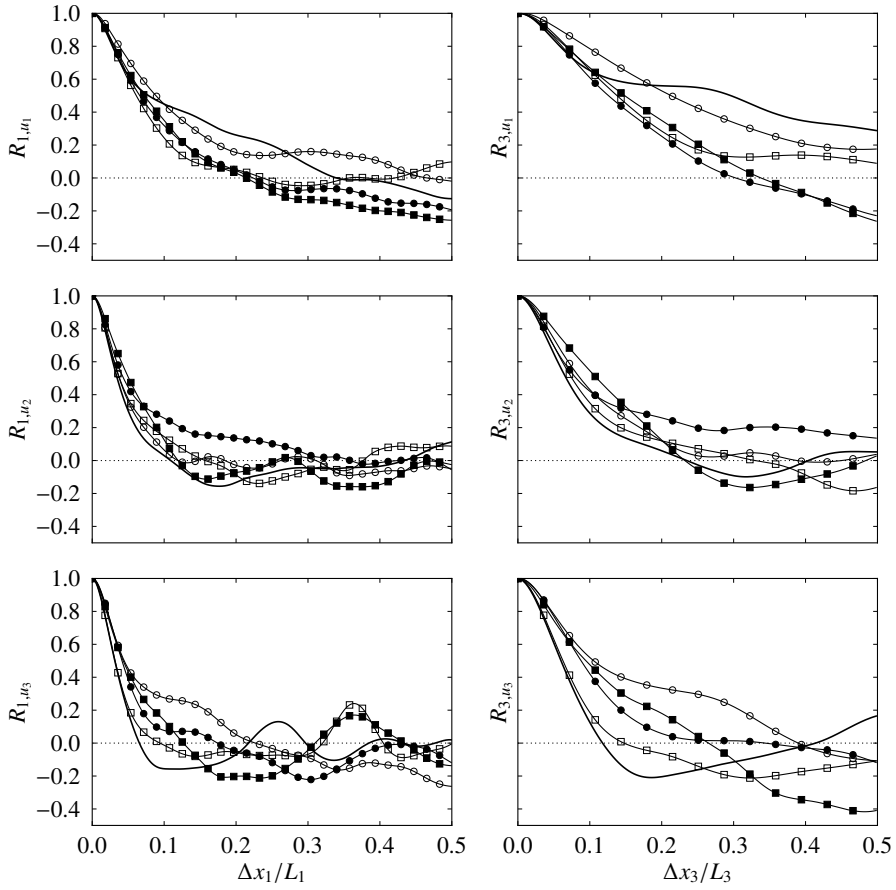

Figure 9: Averaged two-point correlations of the velocity field components. Plain line: center-line. ∘: shearing interface. □: vicinity of the boundary condition. Empty symbols: upper part. Full symbols: lower part.

Another relevant characteristic length is the Taylor micro-scale λ_T. It can be determined from the two-point correlation profiles (Pope, 2000):

$$\lambda_{T,1} = \left(-f_1''(r=0)/2\right)^{-1/2} \quad \text{and} \quad \lambda_{T,3} = \left(-f_3''(r=0)/2\right)^{-1/2} \ , \tag{15}$$

where $f_i = R_{i,u_i}$ for a given value of x_2 and at a given time. In this expression, the notation $''$ represents the second derivative with respect to r, the distance that separates the two points. Considering the osculating parabola p_i of the curve described by f_i leads to:

$$p_i(r) = 1 + r^2 f_i''(0)/2 = 1 - r^2/\lambda_{T,i}^2 \ , \tag{16}$$

from which the value of the Taylor length scale value can be deduced. At this level, it should be pointed out that, for this type of flow configuration (Pope, 2000), the Taylor length scales are inter-related: $\lambda_{T,3} = \lambda_{T,1}/\sqrt{2}$. Figure 10 illustrates the use of the osculating parabola so as to deduce the Taylor scales. For instance, considering the point where the osculating parabola crosses the abscissa axis leads to a value of $\lambda_{T,1}/L_1$ approximately equal to 0.06. The obtained values are reported in the first line of Tab. 5. They are compared to those deduced from the scaling provided below in Eq. (17). The ratio $\lambda_{T,1}/\lambda_{T,3}$ is indeed found to be rather close to $\sqrt{2}$ and this value is better approached using Taylor length scale values issued from the two-point correlations.

	$\lambda_{T,1}/\lambda_{T,3}$	$\lambda_{T,1}/L_1$	$\lambda_{T,3}/L_3$	$\lambda_{T,1}/\Delta x$	$\lambda_{T,3}/\Delta x$
Eq. (16)	1.35	0.056	0.083	31.4	23.2
Eq. (17)	1.24	0.031	0.050	17.4	13.9

Table 5: Comparison of the Taylor micro-scales with respect to computational dimensions.

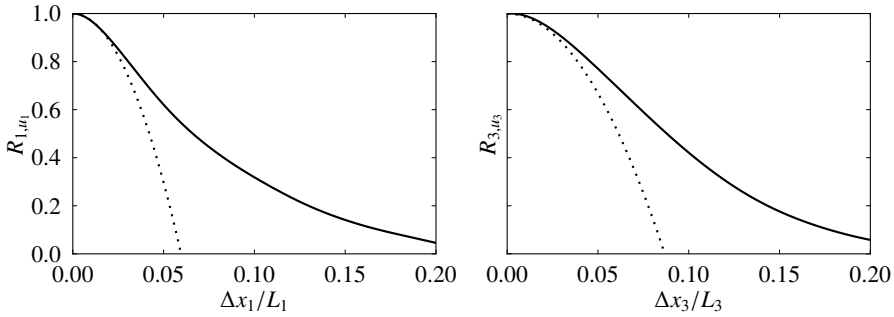

Figure 10: Osculating parabola (dashed line) to two-point correlation profiles (plain line) at point $x_2/\delta_{0.5} = 1.0$.

Based on the turbulent Reynolds number definition $\mathrm{Re}_t = k^{1/2}\ell_t/\nu = k^2/(\varepsilon\nu)$, and considering scalings relevant to HIT, the following expressions can be obtained:

$$\lambda_T/\ell_t = \sqrt{10}\,\mathrm{Re}_t^{-1/2} \quad , \quad \eta_k/\ell_t = \mathrm{Re}_t^{-3/4} \quad \text{and} \quad \lambda_T = \sqrt{10}\,\eta_k^{2/3}\,\ell_t^{1/3} \,, \tag{17}$$

As a computational resolution check, it is worth verifying that the spatial discretization step Δx remains the same order of magnitude as the Kolmogorov scale. In this regard, it must be emphasized that this does not necessarily mean that the ratio $\eta_k/\Delta x$ must be strictly larger than unity (Moin and Mahesh, 1998). The Kolmogorov length scale value is determined using two distinct methods: the first makes use of the resolved mean dissipation rate, see Eq. (12), and the second is based on the two-point correlation used in conjunction with the Kolmogorov scalings, as given by Eq. (17). The resulting values are reported in Tab. 6. The obtained estimates suggest that the level of computational resolution is indeed sufficient and it is also noteworthy that both methods lead to values that are the same order of magnitude.

4. Influence of the dispersed phase

The possible influence of droplet dispersion and vaporization on the flowfield development is now studied on the basis of the three cases `LeU-EV`, `LeU-PEV`, and `LeU-NEV`. Case `LeU-NEV` does not take droplet vaporization into account. Put in other words, the mass and energy couplings between the two phases have not been considered. However, the momentum coupling is maintained. Thus, this case displays some similarities with the particle-laden mixing layers previously studied by Dai et al. (2019a,b). Then, case `LeU-PEV` corresponds to a limit situation where vaporization is assumed to be infinitely fast. The third case `LeU-EV` can be thought as an intermediate situation where vaporization competes with other physical processes. By taking into account different two-way coupling terms, the jet development is expected to differ from one situation to another.

	$\eta_{k,1}/\eta_{k,3}$	$\eta_{k,1}/L_1$	$\eta_{k,3}/L_3$	$\eta_{k,1}/\Delta x$	$\eta_{k,3}/\Delta x$
Eq. (12)	1.06	0.003	0.007	1.94	1.83
Eq. (17)	1.19	0.007	0.011	3.65	3.07

Table 6: Comparison between Kolmogorov length scale estimates and domain dimensions.

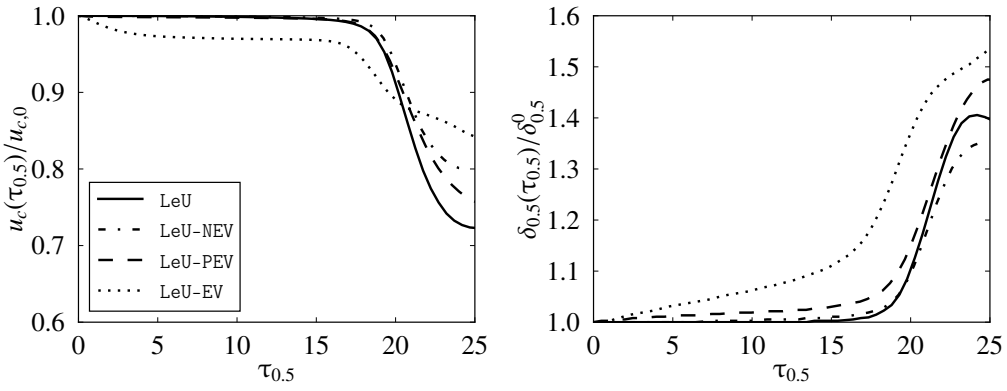

Figure 11: Comparison between temporal evolutions of the normalized convective velocity (left) and half-width (right) obtained for the simulations conducted under the unity-Lewis number approximation.

4.1. Flowfield development

The temporal evolution of the characteristic half-width $\delta_{0.5}$ and convection velocity u_c, as evaluated during the transition and potential core phases, are reported in Fig. 11. The corresponding set of results undoubtedly shows that the influence of the dispersed phase is non-negligible. In this respect, case `LeU-EV` exhibits the largest differences with the reference case `LeU`. In particular, for the convective velocity, a significant decrease is first observed until $\tau_{0.5} = 5$. This is a direct outcome of the evaporation term, indeed, since x_1 and x_3 are homogeneous directions, the transport equation of the mean density reads:

$$\frac{\partial \langle \rho \rangle}{\partial t} = \left\langle \dot{d}_\rho \right\rangle - \frac{\partial \langle \rho u_2 \rangle}{\partial x_2} \, . \tag{18}$$

At the beginning of the simulation, droplets are mostly concentrated within the central part of the jet. Evaporation may take place and it is indeed very effective since, at this location, droplets are the largest and gaseous oxygen mass fraction is the lowest. Thus, the coupling term in Eq. 18 contributes to a density increase at the center of the jet as illustrated in Fig. 12. As further discussed below, the evaporation term also contributes with a positive sign in the momentum budget equation. Nevertheless, since the density increases in the central part of the jet (see the left side of Fig. 12), momentum conservation is achieved through an overall diminution of the jet center-line velocity. At this level, it must be emphasized that, in the momentum transport equation, there is another contribution which does involve the slip velocity between the two phases, see Appendix A. In this respect, it should be recalled that, at the start of the computation, LOx droplets have been randomly scattered within the high-speed central part of the planar jet with no initial slip velocity.

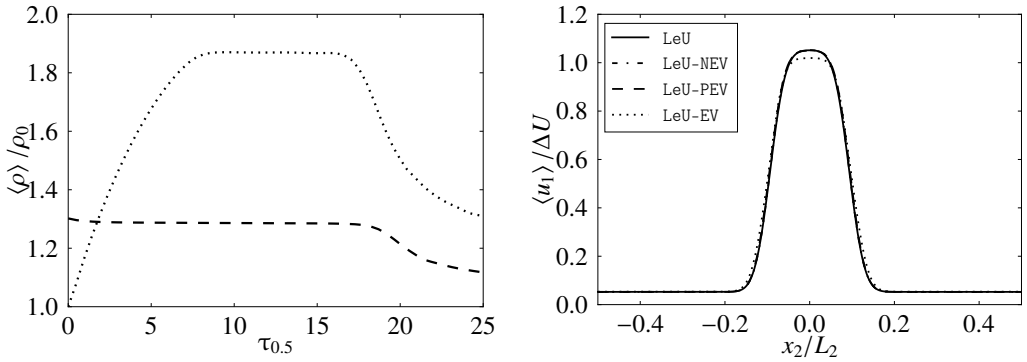

Figure 12: Left: temporal evolution of the normalized density (`LeU-PEV` and `LeU-EV` cases). Right: mean velocity profiles at $\tau_{0.5} = 10$ (`LeU` and `LeU-EV` cases).

At time $\tau_{0.5} = 10$ the computational domain still contains a proportion of around forty-five percent of the initial number droplets. However, ninety-nine percent of the initial liquid mass has already been evaporated. This explains why the convective velocity and density evolutions stabilize after $\tau_{0.5} = 8$. Finally, all droplets are fully evaporated at $\tau_{0.5} = 12$. In the characteristic half-width evolution, two phenomena may be observed. On the one hand, the coupling terms in the momentum equation contribute to the widening of the mean velocity profile. On the other hand, the maximum of the jet convective velocity is decreased in the first phase, thus imposing a lower range for the determination of its characteristic half-width. Therefore, the half-width increases significantly in comparison with the other cases.

To better understand the effects of the dispersed phase on the evolution of the velocity mean profile, the different contributions are now analyzed. The transport equation of the streamwise velocity component may be written as

$$\frac{\partial \langle\rho\rangle \langle u_1\rangle}{\partial t} + \frac{\partial \langle\rho\rangle \langle u_1\rangle \langle u_2\rangle}{\partial x_2} = \frac{\partial \langle\tau_{12}\rangle}{\partial x_2} - \frac{\partial \langle\rho u_1 u_2\rangle - \langle\rho\rangle \langle u_1\rangle \langle u_2\rangle}{\partial x_2} - \frac{\partial \langle\rho u_1\rangle - \langle\rho\rangle \langle u_1\rangle}{\partial t} + \left\langle \dot{d}_{\rho u_1} \right\rangle . \quad (19)$$

The different terms of the RHS of Eq. 19 are, from left to right, the viscous stress term, the term related to the velocity fluctuations, a temporal contribution, and the Eulerian-Lagrangian coupling term. The last one may be decomposed into two distinct contributions: a term related to droplets drag and a source term due to evaporation (see Appendix A).

Figure 13 depicts the contributions of each term during the potential core phase ($\tau_{0.5} = 10$). The corresponding budget is reported in Fig. 14. At this stage of the jet development, the viscous stress term is dominant in most of the cases. It may be observed that both purely gaseous cases feature a similar behavior with only slight differences at the shear layer location, namely $x_2/\delta_{0.5} = \pm 1$. Theses differences

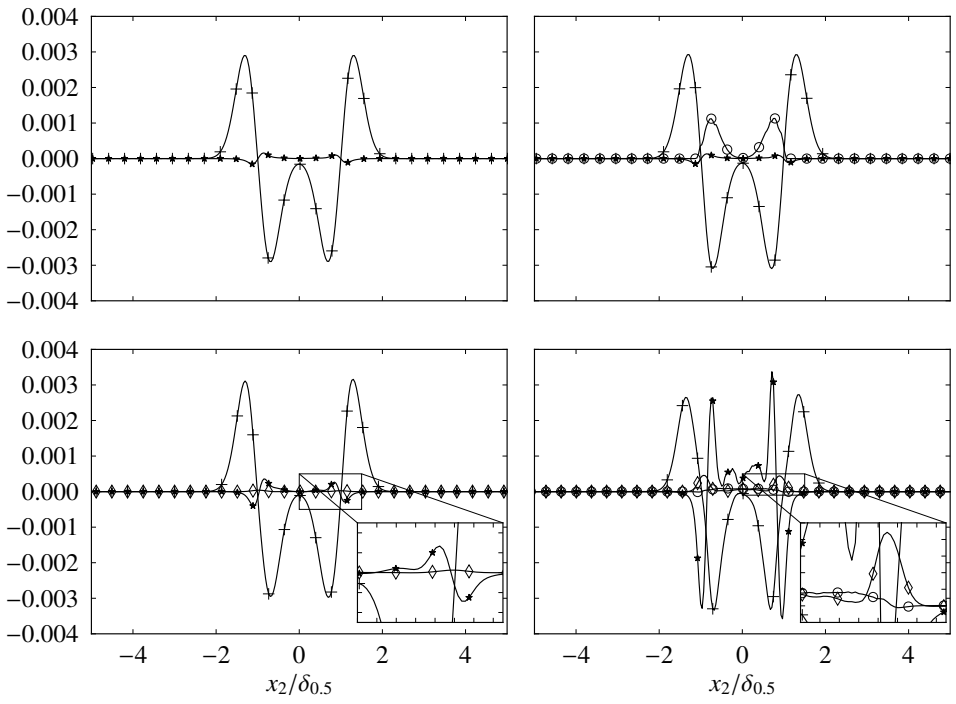

Figure 13: Terms of the stream-wise momentum budget equation, normalized by $\rho_0 \Delta U^2/\delta_{0.5}$, at $\tau_{0.5} = 10$. Upper-left: `LeU`. Upper-right: `LeU-NEV`. Lower-left: `LeU-PEV`. Lower-right: `LeU-EV`. + : Viscous stress. $*$: Velocity fluctuations. $\diamond$: Temporal fluctuations. $\circ$: Eulerian-Lagrangian coupling.

may be ascribed to density fluctuations relevant to the prevaporization of the dispersed phase. In regard to the non-evaporating droplets case, the coupling term related to droplets drag cannot be neglected. In the absence of evaporation, the Stokes number value remains almost unchanged and such that $\mathrm{St} \gg 1$. Therefore, even if the velocity difference between the gas and liquid phases (i.e., the slip velocity) has been initially set to zero, if large velocity fluctuations are triggered in the gas phase, the droplet velocity may be unable to adapt to these variations. Indeed, the drag term is almost zero in the center of the jet since, at this level of development, this zone is almost unaltered by the flowfield inhomogeneity. On the contrary, in the vicinity of the shear layer, where the velocity difference is the largest, the contribution of drag reaches a maximum. Furthermore, because of the positive sign of this contribution in this zone, droplets are prone to maintain large velocity gradients between the jet and the co-flow. This is in agreement with the results previously documented by Ling et al. (2000); Dai et al. (2019b) for particle-laden mixing layers: large particles, i.e., high Stokes number, withdraw kinetic energy to the flow, thus stabilizing the mixing layer, which is in contrast with small particles that enhance momentum exchange and contribute to mixing layer

destabilization.

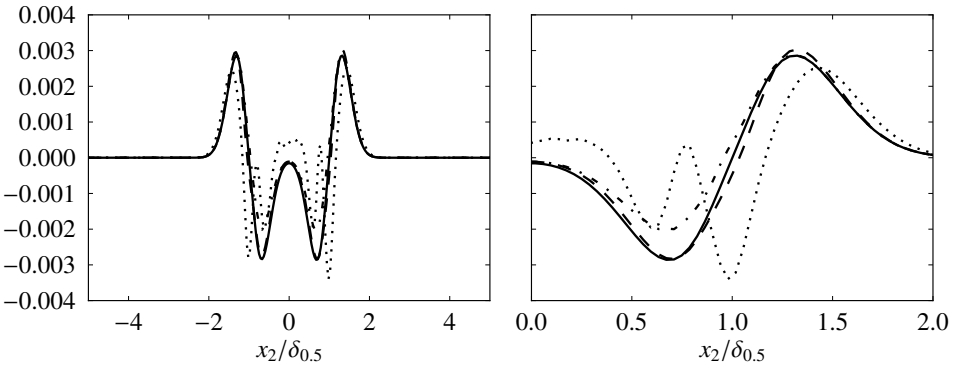

Figure 14: Budget of the stream-wise momentum, normalized by $\rho_0 \Delta U^2/\delta_{0.5}$, at $\tau_{0.5} = 10$ over the whole domain (left) and zoom over $x_2/\delta_{0.5} \leq 2$ (right). Legend: identical to Fig. 11.

As previously stated, case `LeU-EV` features a rather different behavior. In fact, at this level of development, most of the liquid droplets are already evaporated, and hence, the coupling terms are practically negligible with respect to the other terms. Nevertheless, their impact on the flow remains non-negligible through local density and velocity fluctuations that induce a large increase in the fluctuating term. Furthermore, even at this early stage of the jet development, some differences are visible on the centerline. In this respect, the droplet evolution is analyzed through the Stokes number and the Knudsen number Kn as reported in Fig. 15. The latter is defined in a way similar to the work of Kolakaluri et al. (2014) as the ratio $\delta_p/\delta_{0.5}$ between averaged inter-droplet distance δ_p and the flow characteristic length. It should however be emphasized that several definitions of the Knudsen number can be found in the literature, see for instance Fréret et al. (2008). Nevertheless, since no droplet-droplet interaction is taken into account for the dilute conditions considered herein, the definition based on the averaged inter-droplet distance rather than the droplet mean free path seems to be more relevant to the present configuration.

At $\tau_{0.5} = 10$, for case `LeU-NEV`, the PDF of the Stokes number can be approximated by a Dirac delta function. This is in contrast with the PDF obtained for case `LeU-EV`: the kinetic relaxation time, and hence, the Stokes number is markedly decreased because of vaporization. It is indeed noteworthy that most of the droplets are such that St is significantly smaller than unity: droplets are prone to follow the flow streamlines. In regard to the droplet distribution within the computational domain, one can notice that the Knudsen number remains almost unchanged for case `LeU-NEV`: the distribution remains barely modified with respect to the initial one. For case `LeU-EV`, increased values of the Knudsen number are relevant to the increase of

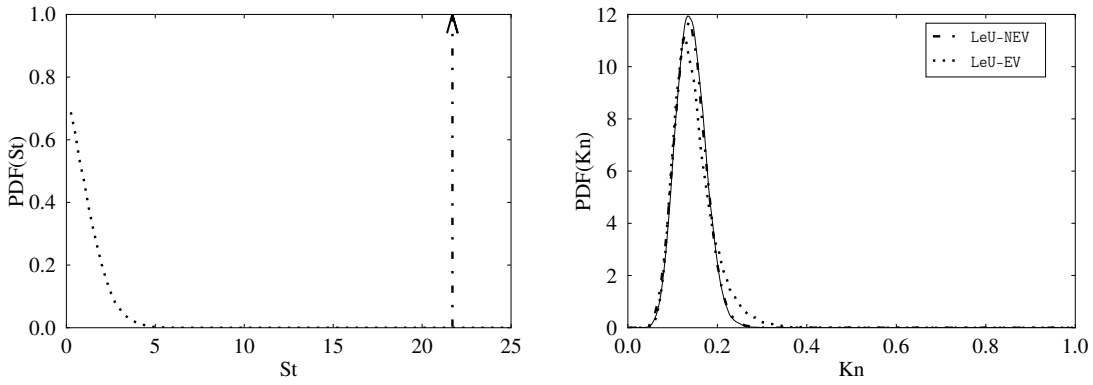

Figure 15: PDF of the Stokes (left) and Knudsen (right) numbers at $\tau_{0.5} = 10$. Plain line: PDF(Kn) at $\tau_{0.5} = 0$.

the droplet inter-distance, which may be as large as half of the half-width. Indeed, some droplets have been already fully evaporated, thus leading to a more dilute spray. Finally, it is usual to scrutinize the possible small-scale inertial clustering that may arise from the competition between the droplet inertia and the Stokes drag, see for instance Wang et al. (2021). Therefore, the droplet Stokes number has been also evaluated on the basis of the dissipative time scale. The PDF of the corresponding Stokes number St_η is reported together with the PDF of the droplet diameter in Fig. 16. Since the Stokes number St_η keeps values larger than unity inertial clustering is not expected to play a significant role.

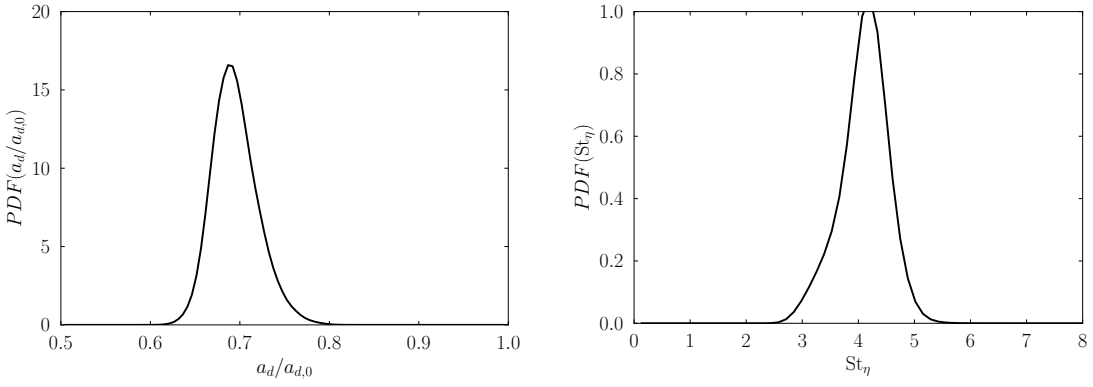

Figure 16: PDF of the normalized droplet diameter (left) and Stokes number St_η (right) at $\tau_{0.5} = 10$ for case `LeU-EV`.

Since the dispersed phase is expected to impact the jet development, the possible self-similarity of the two-phase flow jet is now evaluated for the various conditions that are considered in this section. To this purpose, normalized mean velocity profiles are reported in Fig. 17. In this figure, it is noteworthy that, at

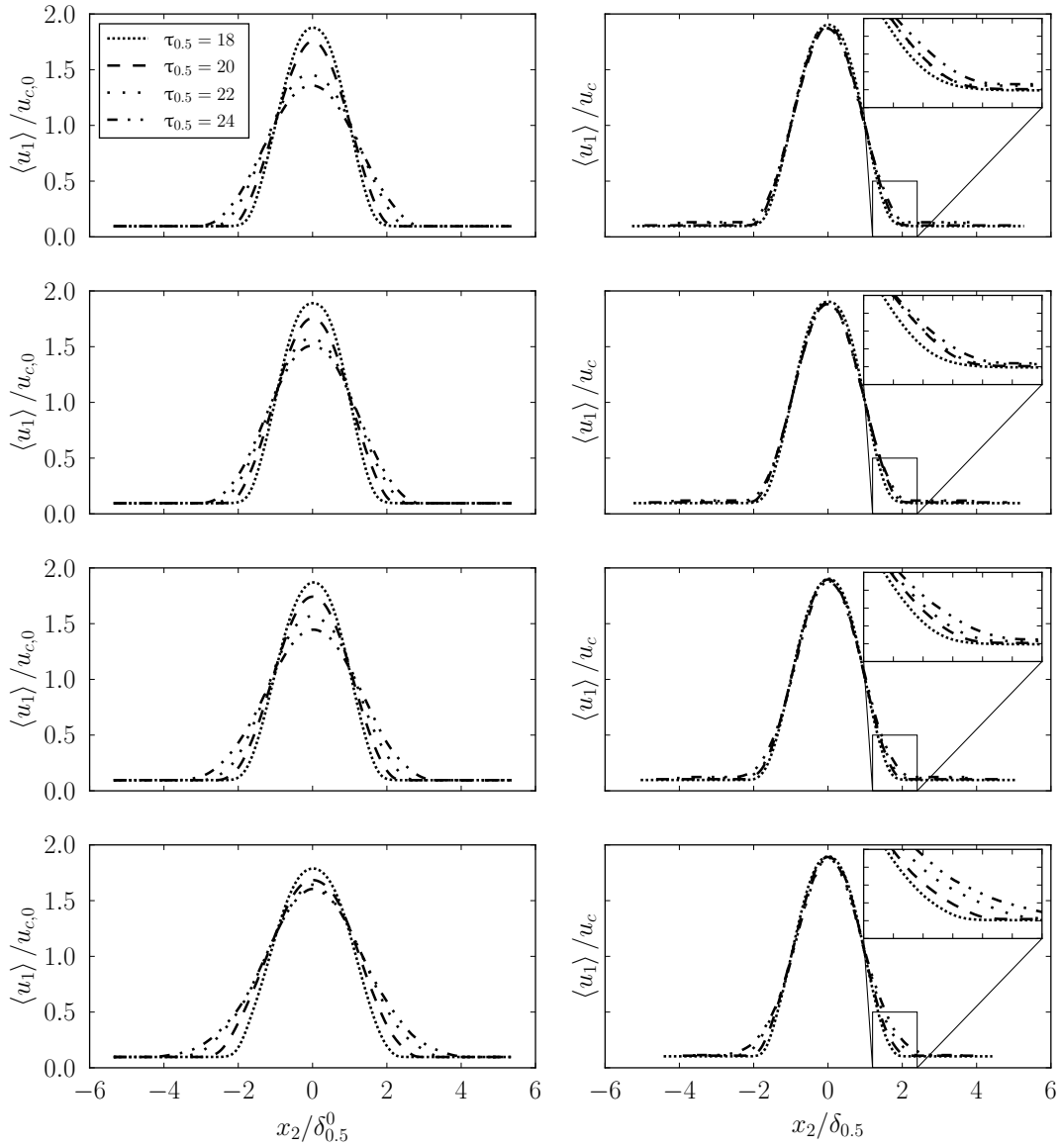

Figure 17: Left: profiles of the mean streamwise velocity component $\langle u_1 \rangle$ plotted versus x_2, values are normalized by the initial half-width and convective velocity. Right: corresponding normalization using the auto-similarity functions. From top to bottom: `LeU`, `LeU-NEV`, `LeU-PEV` and `LeU-EV`.

this level of development, for both configurations featuring no density changes, self-similarity is indeed observed. In regard to the pre-vaporized case, only very slight differences do appear at the bottom of the profiles. In fact, if one except the vaporizing case `LeU-EV`, the results reported in Fig. 17 provide some support to an auto-similar regime for the present conditions. For the case `LeU-NEV`, the fact that there is

no slip velocity at the start of the computations will favor this regime. Finally, as stated above, for case `LeU-EV`, it seems that slight departures from the self-similarity are observed. The results reported on the left side of Fig. 17 show that the width of the normalized mean velocity profiles is larger, even though the decrease of the convective velocity is smaller compared to the other cases.

4.2. Characterization of scalar mixing

In this section, attention is focused on cases `LeU-PEV` and `LeU-EV`. Molecular mixing can take place between the fuel and oxygen vapor. Since diffusivity coefficients are supposed to be the same for all chemical species (i.e., $D_\alpha = D$ for $\alpha = 1, .., N_s$), the various mixture fraction definitions will be equivalent. Therefore, only the results obtained with the Bilger's mixture fraction definition, namely ξ_B as given by Eq. 8, are presented. The joint statistics of the methane mass fraction $Y_{\mathrm{CH_4}}$ and mixture fraction ξ_B obtained at $\tau_{0.5} = 10$ are reported in Fig. 18. As expected, a linear relationship holds between the two variables: the composition of the mixture is unambiguously deduced from the single knowledge of the mixture fraction value.

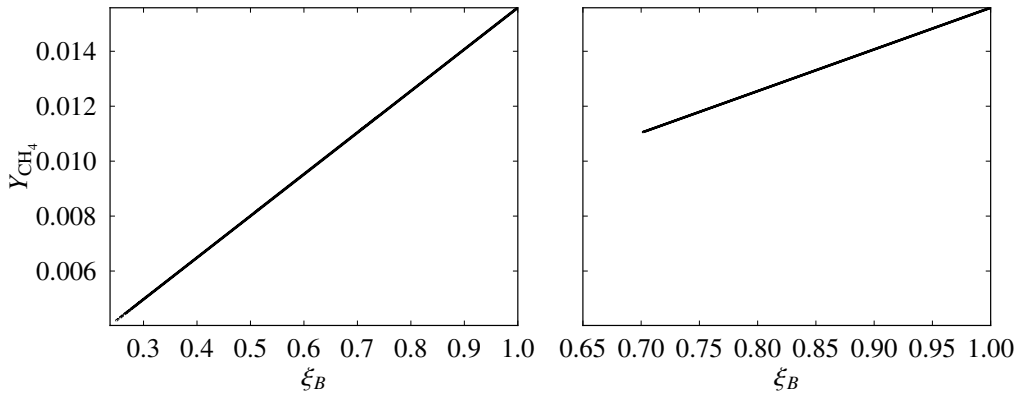

Figure 18: Joint statistics of the CH_4 mass fraction $Y_{\mathrm{CH_4}}$ and mixture fraction ξ_B at $\tau_{0.5} = 10$. Left: `LeU-EV`. Right: `LeU-PEV`.

It is also noteworthy that, for both cases, the oxidizing stream condition (i.e., the point featuring the smallest amount of fuel) differs. This may be further investigated through the mixture fraction PDF, which is reported in Fig. 19. For case `LeU-PEV`, the largest amount of oxidizer is present in the gas phase at $\tau_{0.5} = 0$ and molecular mixing takes place between fuel and the whole amount of oxidizer from $\tau_{0.5} = 0$ to $\tau_{0.5} = 10$. This is in contrast with case `LeU-EV`, for which droplets are still evaporating at $\tau_{0.5} = 10$ thus leading to regions featuring larger concentrations of oxygen. At this level, it seems worth pointing out that pure oxidizer conditions are never reached in the gas phase.

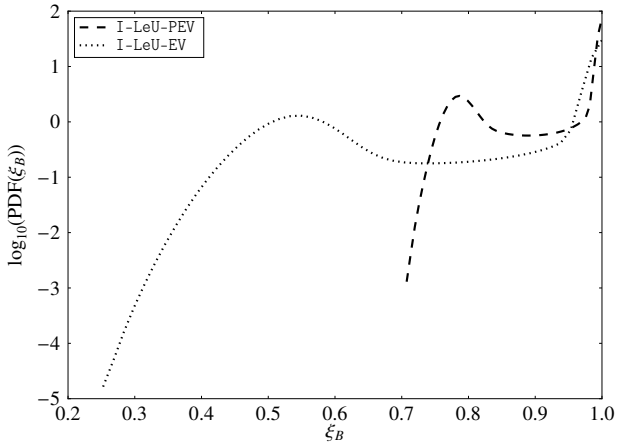

Figure 19: PDF of the mixture fraction ξ_{B} at $\tau_{0.5} = 10$.

The mixing rates are now inspected on the basis of the mixture fraction scalar dissipation rate (SDR), which is defined as $\chi = 2\,D\,\mathbf{g}_\xi \cdot \mathbf{g}_\xi = 2\,D\left\|\mathbf{g}_\xi\right\|^2$, with D the molecular diffusion coefficient of any species and $\mathbf{g}_\xi \equiv \nabla\xi$. The SDR is known to be central to the description of turbulent non-premixed combustion (Gomet et al., 2012) and two-phase flow combustion (Reveillon and Demoulin, 2007), including rocket engine conditions such as those considered herein (Gomet et al., 2014). Figure 20 displays the joint statistics of the scalar dissipation rate χ and mixture fraction ξ_{B} at $\tau_{0.5} = 10$. A non-negligible amount of the statistics corresponds to compositions associated to large values of ξ_{B} (i.e., high concentrations of fuel)

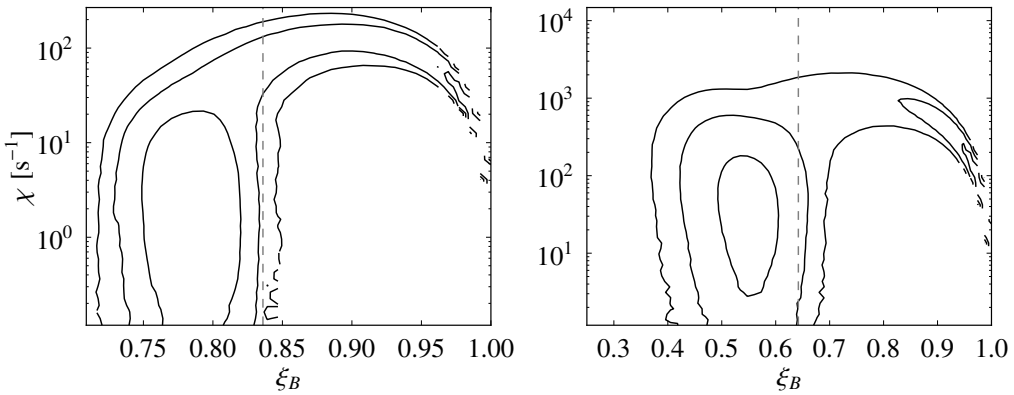

Figure 20: Joint statistics of the scalar dissipation rate χ and mixture fraction ξ_{B} at $\tau_{0.5} = 10$. The difference between each iso-line is one decade. The decade exponents are, from outer to inner: -3, -2, and -1 for case `LeU-PEV` (left), and -4, -3, and -2 for case `LeU-EV` (right). Dashed line: mean mixture fraction.

and rather moderate values of the SDR. In condition LeU-EV the SDR values are significantly increased as smaller values of ξ_B are considered: vaporization sustains composition gradients and associated SDR. Fom a general point of view and, in comparison to case LeU-PEV, SDR levels are indeed significantly larger for condition LeU-EV. Droplet evaporation is an additional source of composition variation and thus enhances the SDR.

4.3. Small-scale analysis

As illustrated in Fig. 21, the birth of the largest structures is triggered at the early stages of the jet development. They feature similar characteristics for all cases. However, significant differences, relevant to the dispersed phase, may be observed: (i) cases LeU and LeU-PEV are indeed quite similar; (ii) for case LeU-NEV the largest structures are significantly reduced in size, and some micro-perturbations located on the vicinity of the droplets may be observed; and (iii) for case LeU-EV, it becomes difficult to discriminate the large-scale structures from micro-perturbations.

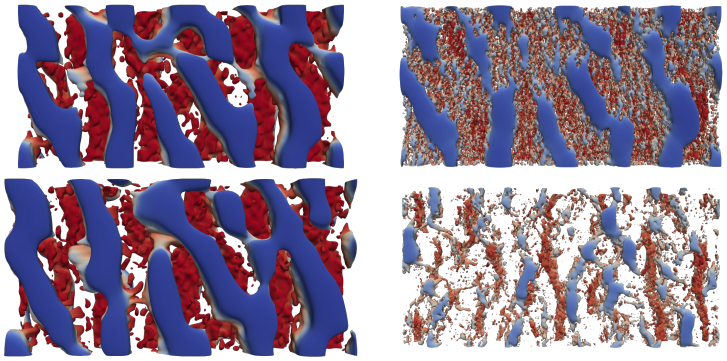

Figure 21: Top view – whole computational domain – of the iso-contour $Q/Q_{max} = 0.01$ colored with the value of the longitudinal velocity component u_1 at $\tau_{0.5} = 10.$. Upper-left: LeU. Upper-right: LeU-NEV. Lower-left: LeU-PEV. Lower-right: LeU-EV.

At latter stages of the jet development, the topology of the flow, as pictured by the Q criterion, are presented in Fig. 22. Configurations LeU and LeU-NEV display rather close characteristics, the main difference being related to the presence of additional micro-perturbations, which are relevant to the dispersed phase. The flow topologies in cases LeU-PEV and LeU-EV seem to display more structures but smaller in size. In particular, a significant number of hairpin-shaped vortices are observed for case LeU-EV and even though all droplets have been evaporated, this may be related to additional vaporization-induced fluctuations.

The joint statistics (Q, R) of the second and third invariants of the VGT obtained at $\tau_{0.5} = 24$ are displayed in Fig. 23. This diagram may be thought of as an illustration of the equilibrium between vorticity

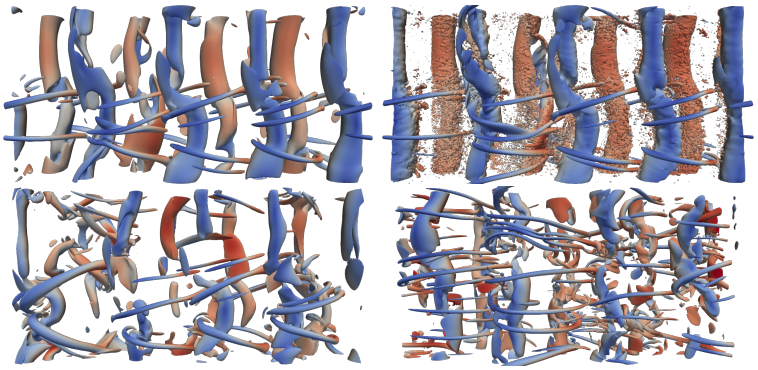

Figure 22: Top view – whole computational domain – of the vortices as identified using the Q-criterion at $\tau_{0.5} = 24$. Iso-surface corresponding to $Q/Q_{\max} = 0.01$ colored with the value of the longitudinal velocity component u_1. Upper-left: `LeU`. Upper-right: `LeU-NEV`. Lower-left: `LeU-PEV`. Lower-right: `LeU-EV`.

production and stretching processes. The condition $Q > 0$ is relevant to vorticity-dominated regions whereas the condition $Q < 0$ corresponds to shear-dominated regions. The meaning of R depends on the sign of Q. For positive values of Q, the negative values of R correspond to compression and vorticity destruction. On the contrary, positives values of R correspond to vorticity production through shearing processes. For negative values of Q, positive values of R are relevant to sheet-like distribution of vorticity whereas negative values correspond to tube-like distribution of vorticity.

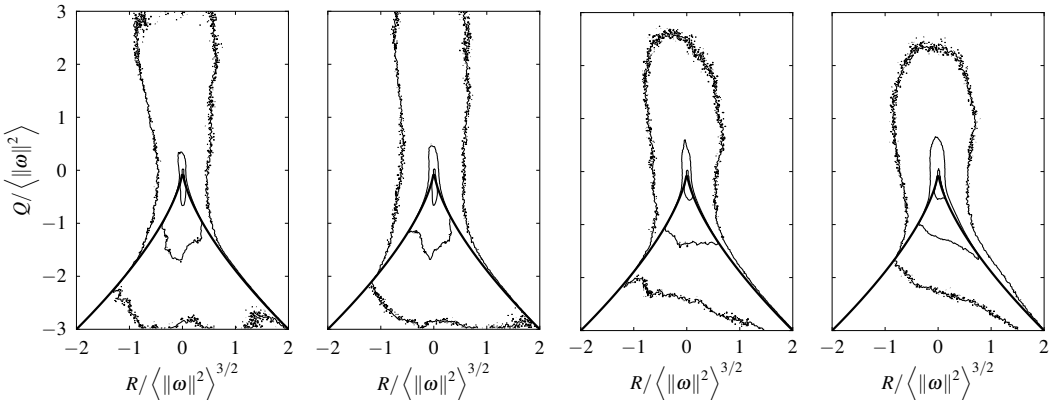

Figure 23: Joint statistics of the invariant Q as a function of R normalized by the norm of the vorticity at $\tau_{0.5} = 24$. The difference between each iso-line is one decade. The decade exponents are, from outer to inner: -2, -1 and 0. From left to right: `LeU`, `LeU-NEV`, `LeU-PEV`, and `LeU-EV`.

Various statistics are observed during the transitional development of the turbulent jet (Gomes-Fernandes et al., 2014; Breda and Buxton, 2019). In cases `LeU` and `LeU-NEV` statistics are dominated by vorticity

($Q > 0$), with equivalent probability of destruction ($R < 0$) and production ($R > 0$). For configurations LeU-PEV and LeU-EV, however, the distributions are closer to those previously reported by Paul and Dodd (2018) in the case of moving bubbles. The shape of the contours stretches along the Vieillefosse line (Vieillefosse, 1982), which characterizes the condition $\Delta = 0$, i.e., zero value of the discriminant of the characteristic polynomial. This may be explained by the presence of pockets featuring significant density variations that impact the flow topology.

As previously mentioned, simulations LeU and LeU-PEV have been conducted until turbulence is developed further downstream. The intermittent nature of the dissipation rate in turbulent flows suggests that its distribution is rather close to a log-normal function (Wang et al., 1996). Figure 24 displays the standardized turbulence dissipation rate and scalar dissipation rate for these two cases. For the sake of consistency, only the regions where turbulence tends towards an homogeneous stage are considered. Thus, the statistical analysis is conditioned to the half-width $|x_2/\delta_{0.5}| \leq 1$. In addition to this, the corresponding statistical moments are reported in Tab. 7. Here, the notations $\sigma(\bullet)$, $\sigma(\bullet)^2$, and $\mu_r(\bullet)$ stand for the standard deviation, the variance, and the r-th order moment, respectively.

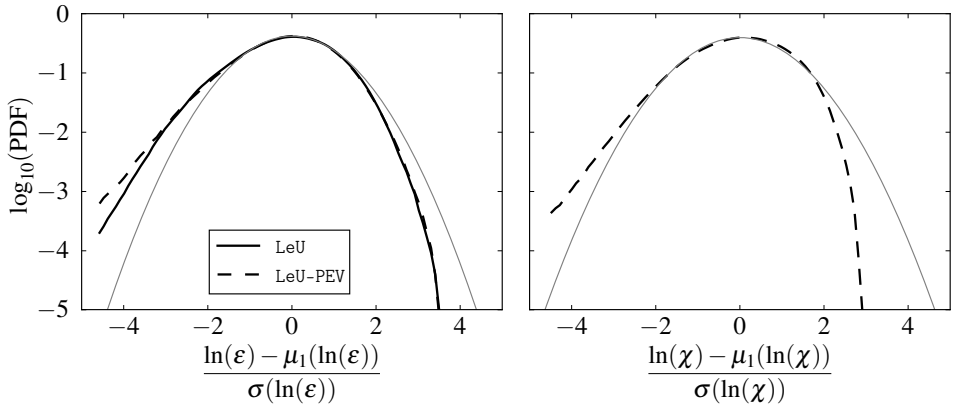

Figure 24: Standardized PDF of $\ln(\varepsilon)$ (left) and $\ln(\chi)$ (right) conditioned to the half-width $|x_2/\delta_{0.5}| \leq 1$. Gray line: Gaussian distribution.

For comparison, a reference Gaussian distribution is also provided in both figures. It may be observed that for all retained quantities, the distribution is rather close to a log-normal. This behavior is indeed observed for different flow configurations studied in the literature (Vedula et al., 2001). In fact, a "super-Gaussian" behavior is observed on the left side whereas a "sub-Gaussian" behavior is observed on the right side. This corresponds to a negative but small skewness (μ_3) and a kurtosis (μ_4) close to 3, which is the

505 characteristic value of a Gaussian distribution. Finally, it may be observed that the departure from the log-normal behavior is more important for configuration `LeU-PEV`.

	ε (LeU)	ε (LeU-PEV)	χ
$\sigma(\bullet)/\mu_1(\bullet)$	1.18	1.22	1.93
$\mu_3(\bullet)$	3.75	4.10	5.03
$\mu_4(\bullet)$	30.2	35.3	43.4
$\sigma(\ln(\bullet))^2$	1.19	1.24	3.03
$\mu_3(\ln(\bullet))$	−0.34	−0.41	−0.38
$\mu_4(\ln(\bullet))$	3.15	3.45	3.20

Table 7: Statistical moments of the turbulence and scalar dissipation rates conditioned to the jet half-width.

5. Influence of the molecular transport model

The unity Lewis number assumption is standardly retained to describe mixing processes taking place in multicomponent flows. Its validity however remains questionable from a general point of view, as previously
510 shown, for instance, in the analyses of Ranga Dinesh et al. (2016) and Falkenstein et al. (2020b,a). In this respect, differential diffusion effects have been shown to alter the SDR at turbulent interface in temporally-developing plane jet (Hunger et al., 2016). This section is focused on this peculiar issue with special emphasis placed on the choice of a relevant molecular transport model for the present configuration.

5.1. Flowfield development

515 Figure 25 reports a comparison between the temporal evolutions of the characteristic convective velocity and half-width obtained for cases `LeU-PEV` and `LeU-EV`, and for the corresponding configurations that takes differential diffusion effects into account, namely cases `LeNU-PEV` and `LeNU-EV`. This figure shows that the impact of differential diffusion seems to be less important than the one relevant to the presence of a dispersed phase. However, it should be pointed out that its overall effect on the flow is non-negligible.

520 To make the discussion easier, the ratio between the molecular diffusivity of the chemical species injected at the liquid state (O_2) and thermal diffusivity, which is nothing else but $1/\mathrm{Le}_{O_2}$ is reported in Fig. 26. The corresponding profile has been obtained at $\tau_{0.5} = 10$ and it results from an averaging performed along homogeneous directions, i.e., planes (x_1, x_3). First, it is remarkable that, even if the differences with respect to the profile relevant to the unity Lewis number assumption are indisputable, the ratio between the oxygen

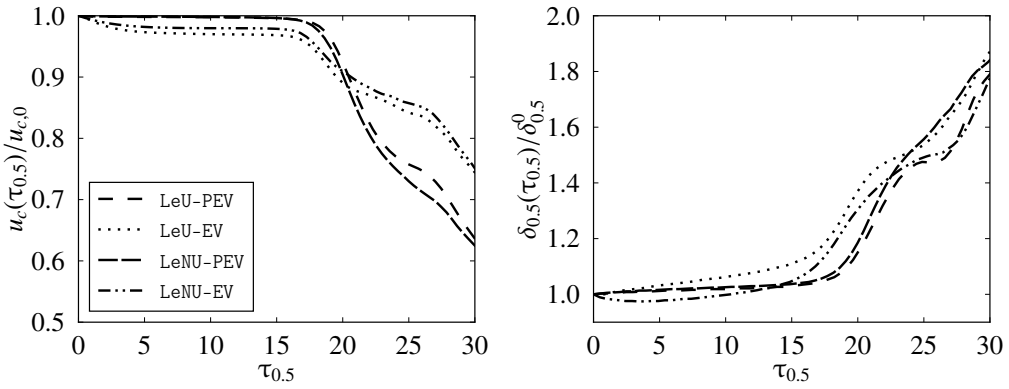

Figure 25: Comparison between the temporal evolutions of the convective velocity and the half-width obtained for cases `LeU-PEV`, `LeU-EV`, `LeNU-PEV`, and `LeNU-EV`.

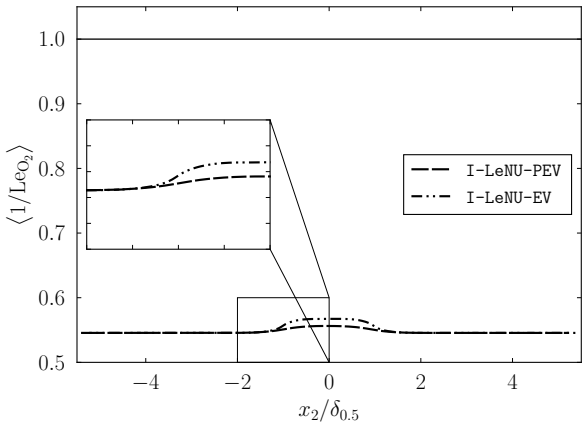

Figure 26: Profiles of the mean value of the oxygen Lewis number obtained for cases `LeNU-PEV` and `LeNU-EV`. The plain line corresponds to the standard unity Lewis number approximation.

diffusivity and the thermal diffusivity remains almost constant across the whole jet. The slight variations that are observed may be simply ascribed to changes in temperature and composition. In this regard, a common approach consists in imposing a constant Lewis number for all chemical species. However, it is also important to point out that the droplet evaporation rate is directly related to the molecular diffusivity coefficient. Indeed, for a given mixture composition (and provided one assumes negligible variations of the Sherwood number), droplet evaporate twice as fast in the unity Lewis number case `LeU-EV` than they do in the differential diffusivity case `LeNU-EV`. For instance, at time $\tau_{0.5} = 10$, half of the total number of droplets as well as ninety-nine percent of the injected liquid mass has been evaporated in case `LeU-EV`,

whereas in case LeNU-EV all droplets are still present and only seventy percent of the total mass has been evaporated. Hence, it is expected that droplet evaporation is less intense and lasts over a longer period of the jet development in the second case.

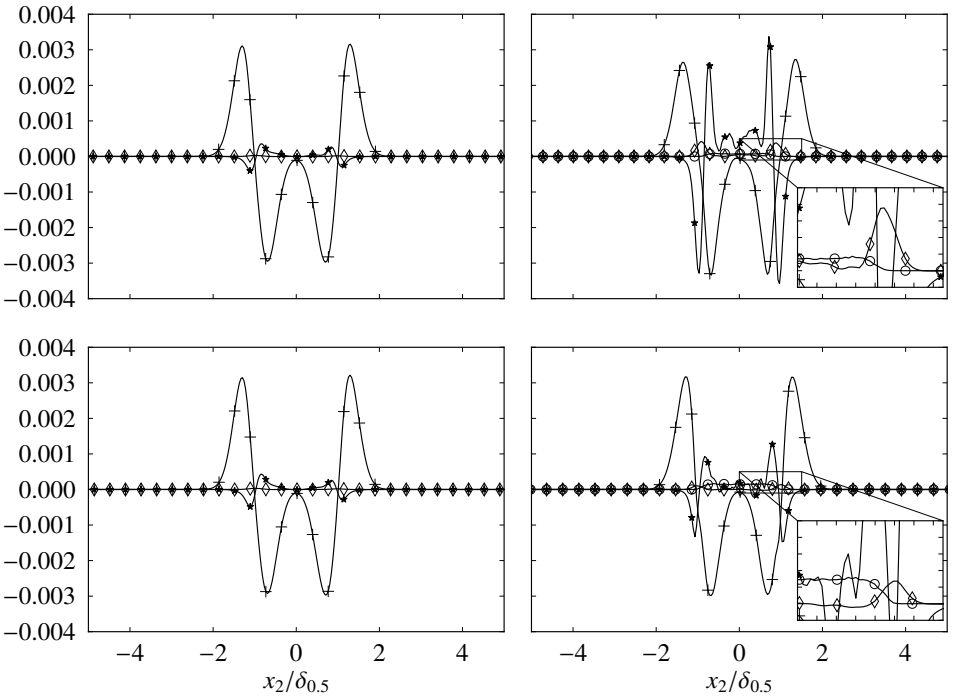

Figure 27: Terms of the mean velocity budget normalized by $\rho_0 \Delta U^2/\delta_{0.5}$ at $\tau_{0.5} = 10$. Upper-left:LeU-PEV. Upper-right: LeU-EV. Lower-left: LeNU-PEV. Lower-right: LeNU-EV. + : viscous stress. $*$: velocity fluctuations. $\diamond$: temporal fluctuations. $\circ$: Eulerian-Lagrangian coupling.

To get further insights into the mean velocity evolution, the various terms present in its transport equation, as well as the budget itself, are reported in Figs. 27 and 28, respectively. It seems that differential diffusivity does not significantly influence the jet development in gaseous conditions. Indeed, both pre-vaporized cases LeU-PEV and LeNU-PEV feature close characteristics. This is in contrast with evaporating cases LeU-EV and LeNU-EV, which display noticeable differences. These differences are direct outcomes of evaporation through the Eulerian-Lagrangian coupling terms and temporal variations of density. The former is more important in case LeNU-EV since, at the considered stage of development, the liquid volume fraction is larger. The second term is more important in case LeU-EV, and as previously emphasized, this may be explained by the more abrupt evaporation in this case, which leads to higher density fluctuations. The various terms are almost the same for both pre-vaporized cases. However, both evaporating cases dis-

play additional variations compared to their pre-vaporized counterparts. These variations remain moderate

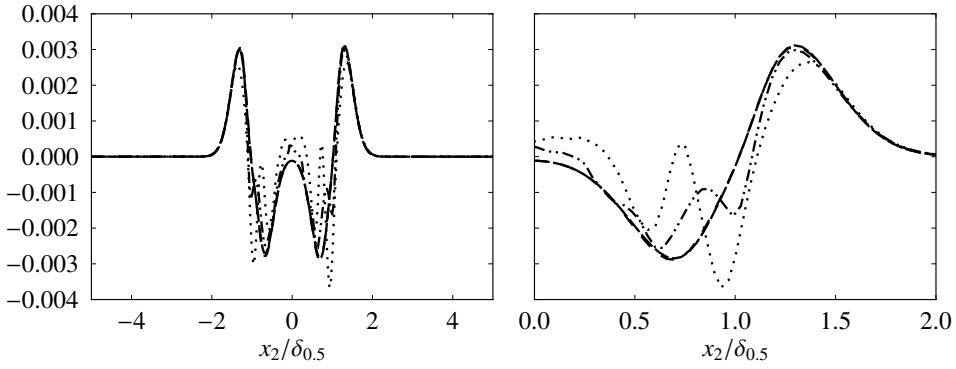

Figure 28: Budget of the streamwise momentum, normalized by $\rho_0 \Delta U^2/\delta_{0.5}$, at $\tau_{0.5} = 10$ over the whole domain (left) and zoom over $x_2/\delta_{0.5} \leq 2$ (right). Linestyles are the same as those used in Fig. 25.

for case `LeNU-EV` whereas they are significant in case `LeU-EV`. Therefore, these two jet configurations are expected to develop in a different manner. Differences in evaporation rate obviously impact the droplet size distributions. Figure 29 reports the PDF of the Knudsen and Stokes numbers at $\tau_{0.5} = 10$. It may be observed that for case `LeU-EV`, droplets are more dispersed. This may be explained by (i) a higher dilution rate and (ii) Stokes number values smaller than unity for a significant proportion of the droplets. Moreover,

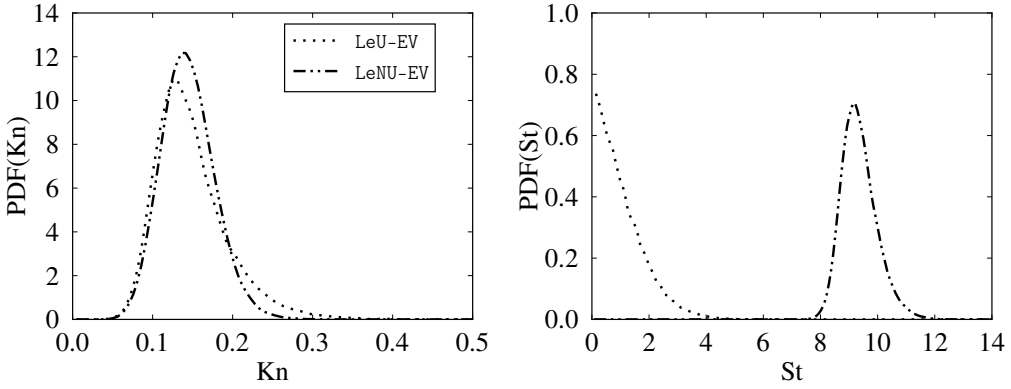

Figure 29: PDF of the Knudsen (left) and Stokes (right) numbers at $\tau_{0.5} = 10$ for cases `LeU-EV` and `LeNU-EV`.

even if the droplet Stokes number is decreased for case `LeNU-EV`, it remains larger than unity. Thus, the kinetic relaxation time is higher than the flow characteristic time, and hence, the distribution of droplets in the computational domain is not significantly altered.

Cross-stream profiles of the normalized longitudinal velocity component and possible self-similarity characteristics are now analyzed. The right side of Fig. 30 displays mean velocity profiles for cases LeNU-PEV and LeNU-EV, once normalized by u_c and $\delta_{0.5}$. It is noteworthy that, after normalization, these profiles are not perfectly superimposed, especially for the case with evaporation (LeNU-EV). The discrepancies observed in case LeNU-EV increase with time but remain however quite similar to those reported in the previous section for case LeU-EV.

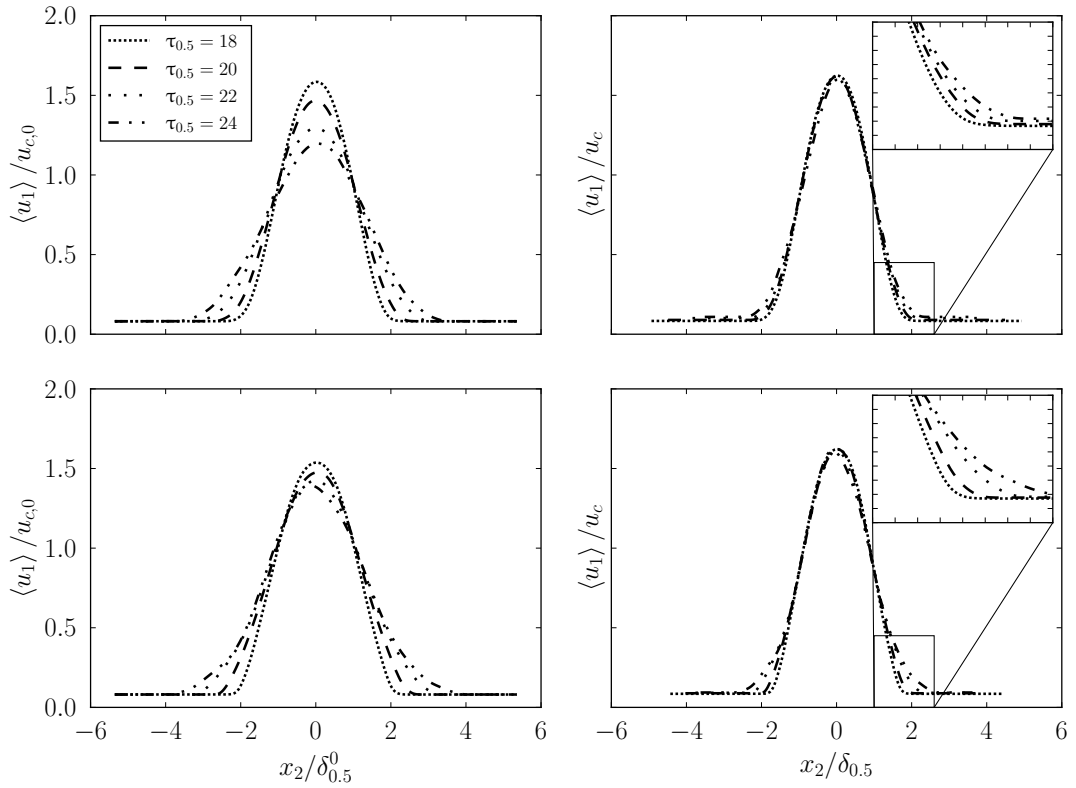

Figure 30: Left: profiles of the mean streamwise velocity component $\langle u_1 \rangle$ plotted versus x_2, values are normalized by the initial half-width and convective velocity. Right: normalization using the auto-similarity functions $u_c(t)$ and $\delta^0_{0.5}(t)$. Top: LeNU-PEV. Bottom: LeNU-EV.

5.2. Description of the multicomponent mixture

Under the unity Lewis number assumption, the composition of the fresh mixture is unequivocally described by the mixture fraction. This quantity is of particular interest in the framework of either non-premixed or partially-premixed combustion (Mura and Demoulin, 2007; Gomet et al., 2012). For instance, the flamelet framework relies on the knowledge of this mixture fraction field together with associated

SDR (Peters, 1984). Therefore, a suitable mixture fraction definition is required to proceed with the description of the turbulent reactive flow within this modelling framework. Figure 31 depicts, for the case `LeNU-EV`, iso-lines of the joint PDF of (i) mixture fraction and methane mass fraction and (ii) mixture fraction and oxygen mass fraction. The two definitions introduced in section 2.3 are considered. As expected, since differential diffusion effects are now taken into account, non-negligible departures from linearity are observed.

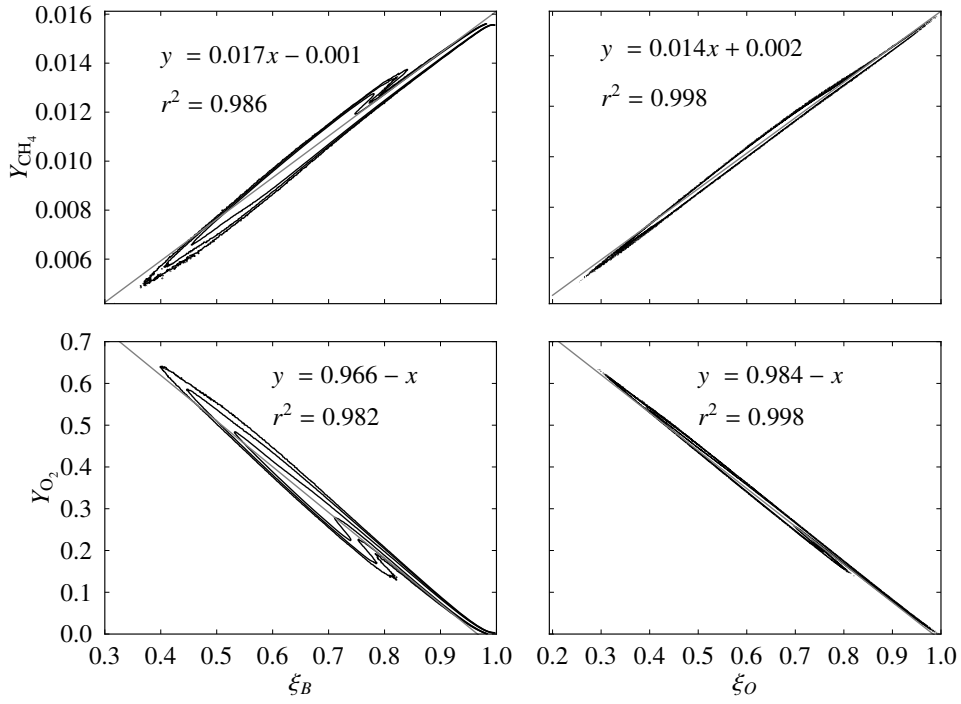

Figure 31: Iso-lines of the joint PDF of (i) mixture fraction and methane mass fraction (top) and (ii) mixture fraction and oxygen mass fraction (bottom) at $\tau_{0.5} = 10$ for case `LeNU-EV`. Two definitions of the mixture fraction are considered: ξ_{B} (left) and ξ_{O} (right). The difference between each iso-line is one decade. The decade exponents are, from outer to inner: 0, 1 and 2 for $Y_{\mathrm{CH_4}}$, and -1, 0 and 1 for $Y_{\mathrm{O_2}}$. Gray line: linear behaviour.

It is noteworthy that the mixture fraction definition based on oxygen atoms conservation ξ_{O} seems to be a better candidate to describe the multicomponent mixture since it leads to a relationship between composition (i.e., chemical species mass frations) and mixture fraction that is closer to linearity and univocality. This behaviour may be related to the characteristics of the retained configuration. Indeed, the oxygen that is delivered in the gas phase through LOx droplets vaporization is easier to follow through the ξ_{O} definition.

Moreover, as emphasized in the previous sections, the evaporation rate is driven to a large extent by

molecular transport and modifications in evaporation rate directly impact the composition of the gaseous mixture. This is illustrated on the mixture fraction PDF reported in Fig. 32. At this level, it must be pointed out that, in order to consider only regions where molecular mixing is significant, the PDF is conditioned by $|x_2/\delta_{0.5}| < 2$ for the early stage of the jet development ($\tau_{0.5} = 10$) and $|x_2/\delta_{0.5}| < 4$ for the latter stage ($\tau_{0.5} = 24$).

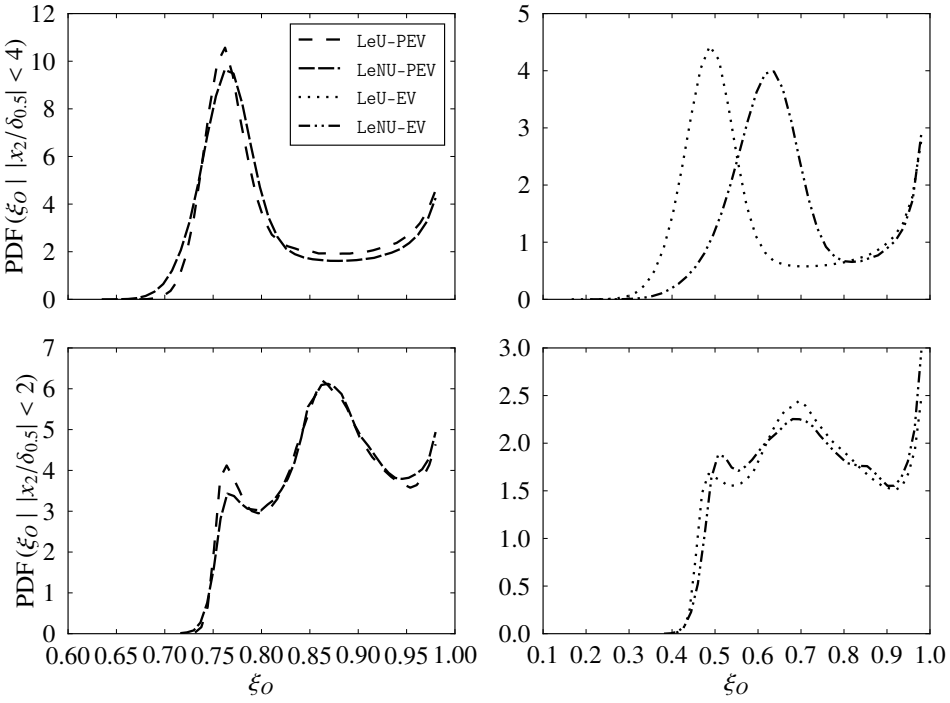

Figure 32: Conditioned PDF of the mixture fraction at $\tau_{0.5} = 10$ (top) and $\tau_{0.5} = 24$ (bottom).

For the pre-vaporized cases, the influence of differential diffusion remains moderate but cannot be neglected. Indeed, the presence of fuel-lean zones is slightly increased in case `LeNU-PEV` compared to case `LeU-PEV`. This may be explained by the smaller value of the molecular diffusion coefficient of oxygen associated to case `LeNU-PEV`. This is in contrast with the vaporizing cases: since vaporization is intensified in case `LeU-EV`, larger amounts of oxygen are present at the early stages of the jet development. Once the jet has developed over a longer time, these differences are lessened. Finally, the results show that, even if differential diffusion has a moderate direct impact on the jet development, its effects on vaporization may however be significant. Thus, scalar fields may be significantly altered compared to their counterparts obtained under the unity-Lewis number approximation and, as a consequence, in computations of practi-

cal devices featuring liquid injection, non-negligible changes are to be expected when considering (or not) differential diffusion effects.

6. Conclusions and perspectives

This manuscript explores the impact of vaporization and differential diffusion on the development of a temporally evolving droplet-laden plane jet. In a first step of the analysis, a reference case without any droplet is scrutinized. Then, the effects of a vaporizing liquid dispersed phase on the jet development are analyzed. To this purpose, three different configurations, featuring various characteristic evaporation times, are studied. They may be thought of as (i) infinitely fast evaporation – i.e., pre-vaporized –, (ii) infinitely slow evaporation – i.e., non-evaporating –, and (iii) finite-rate evaporation competing with convective and molecular processes. It is found that the impact of the dispersed phase on the jet development cannot be neglected, especially in the case featuring finite values of the droplet vaporization time, which leads to the largest modifications with respect to the reference case. In a third and final step of this study, the influence of the choice of the molecular transport model on the jet development is investigated. It is found that differential diffusion has a rather moderate influence – which cannot however be neglected – on the jet development. The molecular transport model is found to induce significant changes on evaporation, and thus, on the composition. Depending on the application that is considered, as for instance combustion applications, this may have a significant impact of the multicomponent flow development. It is thus concluded that the present DNS databases offer interesting perspective future analyses, considering for instance exothermal reactions taking place among the chemical species.

7. Acknowledgements

This work was granted access to the HPC resources of GENCI (Grand Équipement National de Calcul Intensif)-[CINES/IDRIS] under the allocation DARI A0092B07456.

References

References

Abdelsamie, A., Thevenin, D., 2017. Direct numerical simulation of spray evaporation and autoignition in a temporally-evolving jet. Proceedings of the Combustion Institute 36, 2493–2502. doi:10.1016/j.proci.2016.06.030.

Akiki, G., Moore, W.C., Balachandar, S., 2017. Pairwise-interaction extended point-particle model for particle-laden flows. Journal of Computational Physics 351, 329–357. doi:{10.1016/j.jcp.2017.07.056}.

Balachandar, S., Eaton, J.K., 2010. Turbulent dispersed multiphase flow. Annual Review of Fluid Mechanics 42, 111–133. doi:{10.1146/annurev.fluid.010908.165243}.

Bell, J.H., Mehta, R.D., 1990. Development of a two-stream mixing layer from tripped and untripped boundary layers. AIAA Journal 28, 2034–2042. doi:10.2514/3.10519.

Bernal, L.P., Roshko, A., 1986. Streamwise vortex structure in plane mixing layers. Journal of Fluid Mechanics 170, 499–525. doi:10.1017/S002211208600099X.

Bilger, R.W., 1976. Turbulent jet diffusion flames. Progress in Energy and Combustion Science 1, 87–109. doi:10.1016/0360-1285(76)90022-8.

Bilger, R.W., Starner, S.H., Kee, R.., 1990. On reduced mechanisms for methane-air combustion in nonpremixed flames. Combustion and Flame 80, 135–149. doi:10.1016/0010-2180(90)90122-8.

Bogey, C., 2000. Calcul direct du bruit aérodynamique et validation de modèles acoustiques hybrides. Ph.D. thesis. Ecully, Ecole centrale de Lyon.

Bogey, C., Pineau, P., 2018. Flow and sound fields of low-reynolds-number temporal jets at Mach numbers from 0.3 to 2 (AIAA Paper 2018-3615), in: AIAA/CEAS Aeroacoustics Conference.

Bradbury, L.J.S., 1965. The structure of a self-preserving turbulent plane jet. Journal of Fluid Mechanics 23, 31–64. doi:10.1017/S0022112065001222.

Bradbury, L.J.S., Riley, J., 1967. The spread of a turbulent plane jet issuing into a parallel moving airstream. Journal of Fluid Mechanics 27, 381–394. doi:10.1017/S0022112067000400.

Breda, M., Buxton, O.R.H., 2019. Behaviour of small-scale turbulence in the turbulent/non-turbulent interface region of developing turbulent jets. Journal of Fluid Mechanics 879, 187–216. doi:10.1017/jfm.2019.676.

Candel, S., Herding, G., Snyder, R., Scouflaire, P., Rolon, J.C., Vingert, L., Habiballah, M., Grisch, F., Péalat, M., Bouchardy, P., Stepowski, D., Cessou, A., Colin, P., 1998. Experimental investigation of shear-coaxial cryogenic jet-flame. Journal of Propulsion and Power 14, 826–834. doi:10.2514/2.5346.

Capecelatro, J., Desjardins, O., 2013. An Euler–Lagrange strategy for simulating particle-laden flows. Journal of Computational Physics 238, 1–31. doi:{10.1016/j.jcp.2012.12.015}.

Carbajal Carrasco, L.A., 2021. Modélisation et simulation des écoulements turbulents diphasiques réactifs. Ph.D. thesis. Ecole Nationale Supérieure de Mécanique et d'Aérotechnique (ENSMA), Poitiers (France).

Comte, P., Lesieur, Perry, M., Chollet, J.P., 1986. Numerical simulations of vortices in mixing layers and plane jets. Fluid Dynamics Research 3, 315–319. doi:10.1016/0169-5983(88)90084-6.

Cook, A.W., Riley, J.J., 1996. Direct numerical simulation of a turbulent reactive plume on a parallel computer. Journal of Computational Physics 129, 263–283. doi:{10.1006/jcph.1996.0249}.

Crowe, C.T., Sharma, M.P., Stock, D.E., 1977. The particle-source-in cell (PSI-CELL) model for gas-droplet flows. Journal of Fluids Engineering 99, 325–332. doi:10.1115/1.3448756.

Cucitore, R., Quadrio, M., Baron, A., 1999. On the effectiveness and limitations of local criteria for the identification of a vortex. European Journal of Mechanics - B/Fluids 18, 261–282. doi:https://doi.org/10.1016/S0997-7546(99)80026-0.

Dai, Q., Jin, T., Luo, K., Fan, J., 2019a. Direct numerical simulation of a three-dimensional spatially evolving compressible mixing

layer laden with particles. I. Turbulent structures and asymmetric properties. Physics of Fluids 31, 083302. doi:10.1063/1.5099469.

Dai, Q., Jin, T., Luo, K., Xiao, W., Fan, J., 2019b. Direct numerical simulation of a three-dimensional spatially evolving compressible mixing layer laden with particles. II. Turbulence anisotropy and growth rate. Physics of Fluids 31, 083303. doi:10.1063/1.5110990.

Demoulin, F.X., Zurbach, S., Mura, A., 2009. High pressure supercritical turbulent cryogenic injection and combustion: a single-phase flow modeling proposal. Journal of Propulsion and Power 25, 452–464. doi:10.2514/1.36948.

Dubief, Y., Delcayre, F., 2000. On coherent-vortex identification in turbulence. Journal of turbulence 1, 011. doi:10.1088/1468-5248/1/1/011.

Esmaily, M., Horwitz, J.A.K., 2018. A correction scheme for two-way coupled point-particle simulations on anisotropic grids. Journal of Computational Physics 375, 960–982. doi:{10.1016/j.jcp.2018.09.009}.

Falgout, R.D., Yang, U.M., 2002. HYPRE: A library of high performance preconditioners, in: International Conference on Computational Science, Springer. pp. 632–641.

Falkenstein, T., Chu, H., Bode, M., Kang, S., Pitsch, H., 2020a. The role of differential diffusion during early flame kernel development under engine conditions – part II: Effect of flame structure and geometry. Combustion and Flame 221, 516–529. doi:10.1016/j.combustflame.2020.06.002.

Falkenstein, T., Rezchikova, A., Langer, R., Bode, M., Kang, S., Pitsch, H., 2020b. The role of differential diffusion during early flame kernel development under engine conditions. Part I: Analysis of the heat-release-rate response. Combustion and Flame 221, 502–515. doi:10.1016/j.combustflame.2020.06.004.

Fréret, L., Laurent, F., de Chaisemartin, S., Kah, D., Fox, R.O., Vedula, P., Reveillon, J., Thomine, O., Massot, M., 2008. Turbulent combustion of polydisperse evaporating sprays with droplet crossing: Eulerian modeling of collisions at finite knudsen and validation, in: Center for Turbulence Research Proceedings of the Summer Program, pp. 277–288.

Fu, S., Li, Q., 2006. Numerical simulation of compressible mixing layers. International Journal of Heat and Fluid Flow 27, 895–901. doi:10.1016/j.ijheatfluidflow.2006.03.028.

Germes Martinez, L., Duret, B., Reveillon, J., Demoulin, F.X., 2023. Vapor mixing in turbulent vaporizing flows. International Journal of Multiphase Flow 161, 104388. doi:{10.1016/j.ijmultiphaseflow.2023.104388}.

Gomes-Fernandes, R., Ganapathisubramani, B., Vassilicos, J.C., 2014. Evolution of the velocity-gradient tensor in a spatially developing turbulent flow. Journal of Fluid Mechanics 756, 252–292. doi:10.1017/jfm.2014.452.

Gomet, L., Robin, V., Mura, A., 2014. Lagrangian modelling of turbulent spray combustion under liquid rocket engine conditions. Acta Astronautica 94, 184–197. doi:10.1016/j.actaastro.2013.08.016.

Gomet, L., Robin, V., Mura, A., 2015. A multiple-inlet mixture fraction model for nonpremixed combustion. Combustion and Flame 162, 668–687. doi:10.1016/j.combustflame.2014.08.006.

Gomet, L., Robin, V., Mura, V., 2012. Influence of residence and scalar mixing time scales in non-premixed combustion in supersonic turbulent flows. Combustion Science and Technology 184, 1471–1501. doi:10.1080/00102202.2012.690259.

Gordeyev, S.V., Thomas, F.O., 2000. Coherent structure in the turbulent planar jet. Part 1. Extraction of proper orthogonal decomposition eigenmodes and their self-similarity. Journal of Fluid Mechanics 414, 145–194. doi:10.1017/S002211200000848X.

Gordon, S., McBride, B.J., 1976. Computer program for calculation of complex chemical equilibrium compositions, rocket performance, incident and reflected shocks, and Chapman – Jouguet detonations. Technical Report NASA-SP-273. NASA

Lewis Research Center.

Gualtieri, P., Picano, F., Sardina, G., Casciola, C.M., 2013. Clustering and turbulence modulation in particle-laden shear flows. Journal of Fluid Mechanics 715, 134–162. doi:{10.1017/jfm.2012.503}.

Hirschfelder, J.O., Curtiss, C.F., Bird, R.B., Mayer, M.G., 1964. Molecular theory of gases and liquids. volume 165. Wiley New York.

Horwitz, J.A.K., Mani, A., 2016. Accurate calculation of Stokes drag for point–particle tracking in two-way coupled flows. Journal of Computational Physics 318, 85–109. doi:{10.1016/j.jcp.2016.04.034}.

Hu, Z., Luo, X., Luo, K.H., 2002. Numerical simulation of particle dispersion in a spatially developing mixing layer. Theoretical and Computational Fluid Dynamics 15, 403–420. doi:10.1007/s00162-002-0058-9.

Hunger, F., Gauding, M., Hasse, C., 2016. On the impact of the turbulent/non-turbulent interface on differential diffusion in a turbulent jet flow. Journal of Fluid Mechanics 802, R5. doi:10.1017/jfm.2016.471.

Ireland, P.J., Desjardins, O., 2017. Improving particle drag predictions in Euler–Lagrange simulations with two-way coupling. Journal of Computational Physics 338, 405–430. doi:{10.1016/j.jcp.2017.02.070}.

Jeong, J., Hussain, F., 1995. On the identification of a vortex. Journal of Fluid Mechanics 285, 69–94. doi:10.1017/S0022112095000462.

Kolakaluri, R., Subramaniam, S., Panchagnula, M.V., 2014. Trends in multiphase modeling and simulation of sprays. International Journal of Spray and Combustion Dynamics 6, 317–356. doi:10.1260/1756-8277.6.4.317.

Lesieur, M., Metais, O., Comte, P., 2005. Large-eddy simulations of turbulence. Cambridge University Press. doi:10.1017/CBO9780511755507.

Ling, W., Chung, J.N., Crowe, C.T., 2000. Direct numerical simulation of the two-way coupled interaction between particles and mixing layer. Proceedings of the Royal Society of London. Series A: Mathematical, Physical and Engineering Sciences 456, 2931–2955. doi:10.1098/rspa.2000.0647.

Mahle, I., 2007. Direct and large-eddy simulation of inert and reacting compressible turbulent shear layers. Ph.D. thesis. Technische Universität München (Germany).

Majda, A., Sethian, J., 1985. The derivation and numerical solution of the equations for zero Mach number combustion. Combustion Science and Technology 42, 185–205. doi:10.1080/00102208508960376.

Martínez Ferrer, P.J., Lehnasch, G., Mura, A., 2017. Compressibility and heat release effects in high-speed reactive mixing layers. Part I: Growth rates and turbulence characteristics. Combustion and Flame 180, 284–303. doi:10.1016/j.combustflame.2016.09.008.

Moin, P., Mahesh, K., 1998. Direct numerical simulation: a tool in turbulence research. Annual Review of Fluid Mechanics 30, 539–578. doi:10.1146/annurev.fluid.30.1.539.

Mura, A., Demoulin, F.X., 2007. Lagrangian intermittent modelling of turbulent lifted flames. Combustion Theory and Modelling 11, 227–257. doi:10.1080/13647830600967071.

Neophytou, A., Mastorakos, E., Cant, R.S., 2011. Complex chemistry simulations of spark ignition in turbulent sprays. Proceedings of the Combustion Institute 33, 2135–2142. doi:10.1016/j.proci.2010.06.022.

Oefelein, J.C., 2005. Thermophysical characteristics of LOx-H2 flames at supercritical pressure. Proceeding of the Combustion Institute 30, 2929–2937. doi:10.1016/j.proci.2004.08.212.

Onofre Ramos, M.M., Zhao, S., Bouali, Z., Mura, A., 2022a. DNS analysis of turbulent vaporizing two-phase flows. Part I:

Topology of the velocity field. International Journal of Multiphase Flow 156, 104208. doi:10.1016/j.ijmultiphaseflow.2022.104208.

Onofre Ramos, M.M., Zhao, S., Bouali, Z., Mura, A., 2022b. DNS analysis of turbulent vaporizing two-phase flows. Part II: Topology of the scalar field. International Journal of Multiphase Flow 156, 104209. doi:10.1016/j.ijmultiphaseflow.2022.104209.

Ooi, A., Martin, J., Soria, J., Chong, M.S., 1999. A study of the evolution and characteristics of the invariants of the velocity-gradient tensor in isotropic turbulence. Journal of Fluid Mechanics 381, 141–174. doi:10.1017/S0022112098003681.

Pantano, C., Sarkar, S., 2002. A study of compressibility effects in the high-speed turbulent shear layer using direct simulation. Journal of Fluid Mechanics 451, 329–371. doi:10.1017/S0022112001006978.

Pantano, C., Sarkar, S., Williams, F.A., 2003. Mixing of a conserved scalar in a turbulent reacting shear layer. Journal of Fluid Mechanics 481, 291–328. doi:10.1017/S0022112003003872.

Paul, I., Dodd, M.S., 2018. Fine-scale invariants in turbulence generated by rising bubbles, in: Center for Turbulence Research Annual Research Briefs, pp. 65–77.

Peters, N., 1984. Laminar diffusion flamelet models in non-premixed turbulent combustion. Progress in Energy and Combustion Science 10, 319–339. doi:10.1016/0360-1285(84)90114-X.

Pope, S.B., 2000. Turbulent Flows. Cambridge University Press. doi:10.1017/CBO9780511840531.

Ranga Dinesh, K.K.J., Shalaby, H., Luo, K.H., van Oijen, J.A., Thevenin, D., 2016. High hydrogen content syngas fuel burning in lean premixed spherical flames at elevated pressures: effects of preferential diffusion. International Journal of Hydrogen Energy 41, 18231–18249. doi:10.1016/j.ijhydene.2016.07.086.

Rangel, R.H., Sirignano, W.A., 1989. An evaluation of the point-source approximation in spray calculations. Numerical Heat Transfer, Part A: Applications 16, 37–57. doi:{10.1080/10407788908944705}.

Reveillon, J., Demoulin, F.X., 2007. Effects of the preferential segregation of droplets on evaporation and turbulent mixing. Journal of Fluid Mechanics 583, 273–302. doi:10.1017/S0022112007006180.

Reveillon, J., Pera, C., Bouali, Z., 2011. Examples of the potential of DNS for the understanding of reactive multiphase flows. International Journal of Spray and Combustion Dynamics 3, 63–92. doi:10.1260/1756-8277.3.1.63.

Reveillon, J., Vervisch, L., 2005. Analysis of weakly turbulent dilute-spray flames and spray combustion regimes. Journal of Fluid Mechanics 537, 317–347. doi:{10.1017/S0022112005005227}.

Rogers, M.M., Moser, R.D., 1994. Direct simulation of a self-similar turbulent mixing layer. Physics of Fluids 6, 903–923. doi:10.1063/1.868325.

Sadeghi, H., Oberlack, M., Gauding, M., 2018. On new scaling laws in a temporally evolving turbulent plane jet using lie symmetry analysis and direct numerical simulation. Journal of Fluid Mechanics 854, 233–260. doi:10.1017/jfm.2018.625.

Schlichting, H., 1968. Boundary-Layer Theory. McGraw-Hill Book Company. doi:10.1007/978-3-642-85829-1.

Spencer, B.W., Jones, B.G., 1971. Statistical investigation of pressure and velocity fields in the turbulent two-stream mixing layer (AIAA Paper 71-613), in: 4th Fluid and Plasma Dynamics Conference. doi:10.2514/6.1971-613.

Stanley, S.A., Sarkar, S., 1997. Simulations of spatially developing two-dimensional shear layers and jets. Theoretical and Computational Fluid Dynamics 9, 121–147. doi:10.1007/s10494-015-9649-6.

Stanley, S.A., Sarkar, S., Mellado, J.P., 2002. A study of the flow-field evolution and mixing in a planar turbulent jet using numerical simulation. Journal of Fluid Mechanics 450, 377–407. doi:10.1017/S0022112001006644.

Taguelmimt, N., Danaila, L., Hadjadj, A., 2016. Effects of viscosity variations in temporal mixing layer. Flow, Turbulence and Combustion 96, 163–181. doi:10.1007/s10494-015-9649-6.

Townsend, A.A.R., 1956. The structure of turbulent shear flow. Cambridge university press.

Tsinober, A., 2009. An informal conceptual introduction to turbulence. volume 483. Springer.

VanDine, A., Phama, H.P., Sarkar, S., 2020. Investigation of LES models for a stratified shear layer. Computers & Fluids 198, 104405. doi:10.1016/j.compfluid.2019.104405.

Vedula, P., Yeung, P.K., Fox, R.O., 2001. Dynamics of scalar dissipation in isotropic turbulence: a numerical and modelling study. Journal of Fluid Mechanics 433, 29–60. doi:10.1017/S0022112000003207.

Vieillefosse, P., 1982. Local interaction between vorticity and shear in a perfect incompressible fluid. Journal de Physique France 43, 837–842. doi:10.1051/jphys:01982004306083700.

Wang, H., Luo, K., Fan, J., 2014. Effects of turbulent intensity and droplet diameter on spray combustion using direct numerical simulation. Fuel 121, 311–318. doi:10.1016/j.fuel.2013.12.061.

Wang, J., Dalla Barba, F., Picano, F., 2021. Direct numerical simulation of an evaporating turbulent diluted jet-spray at moderate Reynolds number. International Journal of Multiphase Flow 137, 103567. doi:10.1016/j.ijmultiphaseflow.2021.103567.

Wang, L.P., Chen, S., Brasseur, J.G., Wyngaard, J.C., 1996. Examination of hypotheses in the kolmogorov refined turbulence theory through high-resolution simulations. Part 1. Velocity field. Journal of Fluid Mechanics 309, 113—-156. doi:10.1017/S0022112096001589.

Wang, Y., Rutland, C.J., 2007. Direct numerical simulation of ignition in turbulent n-heptane liquid-fuel spray jets. Combustion and Flame 149, 353–365. doi:10.1016/j.combustflame.2007.03.005.

Wygnanski, I., Fiedler, H.E., 1970. The two-dimensional mixing region. Journal of Fluid Mechanics 41, 327—-361. doi:10.1017/S0022112070000630.

Yang, V., 2000. Modeling of supercritical vaporization, mixing and combustion processes in liquid-fueled propulsion systems. Proceeding of the Combustion Institute 28, 925–942. doi:10.1016/S0082-0784(00)80299-4.

Zhao, S., Bouali, Z., Mura, A., 2020. Computational investigation of weakly turbulent flame kernel growths in iso-octane droplet clouds in CVC conditions. Flow, Turbulence and Combustion 104, 139–177. doi:10.1007/s10494-019-00051-x.

Appendix A. Description of the mathematical model

The gas phase is assumed to be a mixture of N_s chemical species. The concentration of each species α is evaluated from its mass fraction $Y_\alpha = \rho_\alpha/\rho$, where ρ refers to the density of the mixture, and ρ_α is the partial density of chemical species α. The energy of the system is characterized on the basis of its sensible enthalpy h_s. The sensible enthalpy of each chemical species is calculated from a reference temperature T_0 using its heat capacity at constant pressure $c_{p,\alpha}$

$$h_{s,\alpha}(T) = \int_{T_0}^{T} c_{p,\alpha}(\theta) d\theta \tag{A.1}$$

which, after summation performed over the whole set of chemical species, leads to

$$h_s(T) = \sum_{\alpha=1}^{N_s} Y_\alpha h_\alpha(T) = \sum_{\alpha=1}^{N_s} \left(Y_\alpha \int_{T_0}^{T} c_{p,\alpha}(\theta) d\theta \right) \tag{A.2}$$

In practice, the thermodynamic properties of each species are determined using the standard seven coefficient polynomials of Gordon and McBride (1976).

The system of equations describing the carrier gas phase may be written as follows

$$\begin{aligned}
\frac{\partial \rho}{\partial t} + \frac{\partial \rho u_j}{\partial x_j} &= \dot{d}_\rho \\
\frac{\partial \rho u_i}{\partial t} + \frac{\partial \rho u_i u_j}{\partial x_j} &= -\frac{\partial p_1}{\partial x_i} + \frac{\partial \tau_{ij}}{\partial x_j} + \dot{d}_{\rho u_i} \\
\frac{\partial \rho h_s}{\partial t} + \frac{\partial \rho u_j h_s}{\partial x_j} &= \frac{\partial p_0}{\partial t} - \frac{\partial q_j}{\partial x_j} + \tau_{ij} \frac{\partial u_i}{\partial x_j} + \dot{d}_{\rho h_s} \\
\frac{\partial \rho Y_\alpha}{\partial t} + \frac{\partial \rho Y_\alpha u_j}{\partial x_j} &= -\frac{\partial J_j^\alpha}{\partial x_j} + \dot{d}_{\rho Y_\alpha}
\end{aligned} \tag{A.3}$$

In the above set of equations, the viscous stress tensor τ_{ij} is evaluated from

$$\tau_{ij} = \mu \left(\frac{\partial u_i}{\partial x_j} + \frac{\partial u_j}{\partial x_i} \right) - \frac{2}{3} \mu \frac{\partial u_k}{\partial x_k} \delta_{ij} \tag{A.4}$$

where μ is the dynamic viscosity and δ_{ij} is the Kronecker symbol. The quantities q_j and J_j^α are the j^{th} components of the heat and species mass flux vectors, respectively. The Hirschfelder and Curtis approximation has been retained to evaluate the molecular diffusion velocity (Hirschfelder et al., 1964) and the expressions of these fluxes components are given by

$$\begin{aligned}
q_j &= -\lambda \frac{\partial T}{\partial x_j} + \sum_{\alpha=1}^{N_s} J_j^\alpha h_{s,\alpha} \\
J_j^\alpha &= \rho Y_\alpha V_j^\alpha = -\rho D_\alpha \frac{\partial Y_\alpha}{\partial x_j} + \rho Y_\alpha \sum_{\beta=1}^{N_s} D_\beta \frac{\partial Y_\beta}{\partial x_j}
\end{aligned} \tag{A.5}$$

where λ is the thermal conductivity of the mixture and D_α is the diffusivity of species α. Finally, it must be emphasized that, in the system A.3, the terms $\dot{d}_\rho$, $\dot{d}_{\rho Y_\alpha}$, $\dot{d}_{\rho u_i}$, and $\dot{d}_{\rho h_s}$ refer to mass, species mass fractions, momentum, and energy coupling terms with the dispersed liquid phase. These various source terms are evaluated from the contributions of each liquid droplet through a volumetric weighted average performed on computational cells in the same way as the one previously described by Reveillon and Vervisch (2005). The expressions of the corresponding terms are provided at the end of this appendix.

In regard to the dispersed phase, liquid droplets are modeled as spherical particles within a Lagrangian framework. Their position, velocity, temperature, and squared diameter are computed from the following set of evolution equations

$$\frac{d\mathbf{X}_d}{dt} = \mathbf{V}_d \tag{A.6}$$

$$\frac{d\mathbf{V}_d}{dt} = \frac{1}{\tau_{V_d}} \left(\mathbf{u}(\mathbf{X}_d, t) - \mathbf{V}_d\right) \tag{A.7}$$

$$\frac{dT_d}{dt} = \frac{1}{\tau_{T_d}} \left(T(\mathbf{X}_d, t) - T_d - \frac{\mathrm{B}_T L_v}{c_p(\mathbf{X}_d, t)} \right) \tag{A.8}$$

$$\frac{da_d^2}{dt} = -\frac{a_d^2}{\tau_{a_d}} \tag{A.9}$$

where $\mathbf{X}_d$, $\mathbf{V}_d$, T_d, and a_d are the droplet coordinates, velocity, temperature, and diameter, respectively. Each droplet is followed through a Lagrangian point of view and assumed to be spherical and at thermodynamical equilibrium. In the above expression, the quantities $\mathbf{u}$, T, and c_p denote the velocity, temperature, and heat capacity at constant pressure of the carrier phase. The quantities B_T and L_v refer to the thermal transfer number and the latent heat of evaporation, respectively. Three droplet characteristic times are involved: the characteristic time of evaporation τ_{a_d}, and the kinetic and temperature relaxation times τ_{V_d} and τ_{T_d}, respectively. They are deduced from the following expressions

$$\tau_{a_d} = \frac{\mathrm{Sc}}{4\,\mathrm{Sh}_c} \frac{\rho_d\, a_d^2}{\mu(\mathbf{X}_d, t)} \frac{1}{\ln(1 + \mathrm{B}_m)} \tag{A.10}$$

$$\tau_{V_d} = \frac{\rho_d\ a_d^2}{18 C_u\, \mu(\mathbf{X}_d, t)} \tag{A.11}$$

$$\tau_{T_d} = \frac{\mathrm{Pr}}{6\,\mathrm{Nu}_c} \frac{\rho_d\, a_d^2}{\mu(\mathbf{X}_d, t)} R_{c_p} \frac{\mathrm{B}_T}{\ln(1 + \mathrm{B}_T)} \tag{A.12}$$

where ρ_d is the liquid phase density and $\mu(\mathbf{X}_d, t)$ is the carrier phase viscosity. The corrective coefficient $C_u = 1 + \mathrm{Re}_d^{2/3}/6$ is introduced to vary the drag factor according to the local droplet Reynolds number $\mathrm{Re}_d = \rho a_d |\mathbf{u}(\mathbf{X}_d, t) - \mathbf{V}_d|/\mu$. The non-dimensional numbers Sc, Pr, Sh_c, and Nu_c denote the Schmidt, Prandtl, Sherwood, and Nusselt numbers, respectively. The quantity $R_{c_p} = C_d/C_p$ refers to the ratio of normalized heat capacities of liquid and gas phases. Finally, the quantity B_m represents the mass flux number, which is evaluated from $\mathrm{B}_m = (Y_L^s - Y_L(\mathbf{X}_d))/(1 - Y_L^s)$, where $Y_L(\mathbf{X}_d)$ is the liquid mass fraction in the vicinity of the droplet, and Y_L^s is the corresponding value at the liquid-gas interface. This value is deduced from the Clausius-Clapeyron saturation law.

Each droplet may have positive or negative contributions to the density, momentum, energy, and chemical species mass fractions transport equations that describe the evolution of the gas phase, see Eq. (A.3),

and the corresponding Lagrangian source terms must be projected onto the Eulerian mesh. For every computational point k, a control volume $\mathcal{V}_k$ is defined on the basis of the mid-distance to the neigboring nodes. Since a homogenous grid of mesh size Δx along the three directions has been used, the corresponding control volume is $\mathcal{V}_k = \Delta x^3$. The mass source term that applies to the computational point k is denoted $\dot{d}_\rho^{(k)}$

$$\dot{d}_\rho^{(k)} = \frac{1}{\mathcal{V}_k} \sum_d \alpha_d^{(k)} \frac{\mathrm{d}\, m_d}{\mathrm{d}t} \tag{A.13}$$

with the sum being performed over every droplet present in the control volume $\mathcal{V}_k$. The quantities $\alpha_d^{(k)}$ are the normalized repartition coefficients of the liquid droplet d on computational node k. Mass, momentum, and energy conservation imposes their sum over k to be unity. Each normalized repartition coefficient is herein defined as the regressive normalized distance between the considered droplet and node. Using Eq. (A.9), and since $m_d = \rho_d \pi a_d^3/6$, the mass source term expression writes

$$\dot{d}_\rho^{(k)} = \rho_d \frac{\pi}{4\mathcal{V}_k} \sum_d \alpha_d^{(k)} \frac{a_d^3}{\tau_{a_d}} \tag{A.14}$$

After some algebra, the momentum and energy source terms that apply to the computational point k are similarly deduced from Eqs. (A.7)-(A.9),

$$\dot{d}_{\rho u_i}^{(k)} = -\rho_d \frac{\pi}{4\mathcal{V}_k} \sum_d \alpha_d^{(k)} a_d^3 \left(\frac{2}{3} \frac{\mathbf{u}(\mathbf{X}_d, t) - \mathbf{V}_d}{\tau_{V_d}} - \frac{\mathbf{V}_d}{\tau_{a_d}} \right) \tag{A.15}$$

$$\dot{d}_{\rho h_s}^{(k)} = -\rho_d C_d \frac{\pi}{4\mathcal{V}_k} \sum_d \alpha_d^{(k)} a_d^3 \left(\frac{2}{3} \frac{T(\mathbf{X}_d, t) - T_d - \mathrm{B}_T L_v / c_p(\mathbf{X}_d, t)}{\tau_{T_d}} + \frac{T_d}{\tau_{a_d}} \right) \tag{A.16}$$

$$\tag{A.17}$$

Finally, since the liquid is pure oxygen, the mass source does also appear as a source term in the oxygen mass fraction transport equation, i.e., $\dot{d}_{\rho Y_{\mathrm{O}_2}}^{(k)} = \dot{d}_\rho^{(k)}$, as given by Eq. (A.14), and $\dot{d}_{\rho Y_\alpha}^{(k)} = 0$ for $\alpha \neq \mathrm{O}_2$.

Appendix B. Flowfield topological characterization

If vorticity $\omega = \nabla \times \mathbf{u}$ has been early considered with the objective of characterizing turbulent flow topology, it should be emphasized that many other relevant quantities have been introduced to proceed with coherent vortices identification (Dubief and Delcayre, 2000). For instance, in the present work, two different criteria are considered. They are based on the velocity gradient tensor (Jeong and Hussain, 1995; Fu and Li, 2006). The first – the Q-criterion – is based on the invariants of the velocity gradient tensor (VGT). The characteristic polynomial of this tensor reads

$$\lambda^3 + P\lambda^2 + Q\lambda + R = 0\,, \tag{B.1}$$

where P, Q, and R denote the three invariants of $\nabla\mathbf{u}$. They are expressed as

$$\begin{aligned} P &= -\nabla\cdot\mathbf{u} = -\operatorname{tr}(\nabla\mathbf{u}) \\ Q &= \frac{1}{2}\left((\nabla\cdot\mathbf{u})^2 - \operatorname{tr}\left(\nabla\mathbf{u}^2\right)\right) = \frac{1}{2}\left(\operatorname{tr}(\nabla\mathbf{u})^2 - \operatorname{tr}\left(\nabla\mathbf{u}^2\right)\right) \\ R &= -\det(\nabla\mathbf{u}) \end{aligned} \tag{B.2}$$

with $\operatorname{tr}(\nabla\mathbf{u})$ and $\det(\nabla\mathbf{u})$ the trace and determinant of the VGT. It is worth emphasizing that, for an incompressible flow, we have $P = 0$. Furthermore, it is noteworthy that Q may be rewritten as follows:

$$Q = \left(\left\|\mathbf{\Omega}^2\right\| - \left\|\mathbf{S}^2\right\|\right)/2\,, \tag{B.3}$$

where $\mathbf{S} = \left(\nabla\mathbf{u} + \nabla\mathbf{u}^T\right)/2$ and $\mathbf{\Omega} = \left(\nabla\mathbf{u} - \nabla\mathbf{u}^T\right)/2$ stand for the symmetric and anti-symmetric parts of the VGT, respectively. The Q-criterion consists in the identification of a coherent vortice by considering an iso-contour $Q > 0$.

The second criterion – the λ-criterion (Jeong and Hussain, 1995) – imposes a condition on the second invariant of tensor $\mathbf{\Omega}^2 + \mathbf{S}^2$. Indeed, this tensor is real and symmetric, and, as a consequence, diagonalizable. Its eigen-values are referred to as λ_1, λ_2, and λ_3, sorted as $\lambda_1 \geq \lambda_2 \geq \lambda_3$. The λ-criterion consists in the identification of zones where $\lambda_2 > 0$. The quantity λ_2 may be related to an equilibrium between stretch and rotation (Cucitore et al., 1999). At this level, it can be pointed out that the invariant Q of $\nabla\mathbf{u}$ may be expressed in terms of eigen-values λ_i, leading to $Q = -(\lambda_1 + \lambda_2 + \lambda_3)/2$.